TÜRKİYE CUMHURİYETİ
ADANA ALPARSLAN TÜRKEŞ SCIENCE AND TECHNOLOGY UNIVERSITY

GRADUATE SCHOOL
NANO TECHNOLOGY AND ENGINEERING SCIENCES DEPARTMENT

INVESTIGATION OF ADVANCED RADAR ABSORBING PANI/YIG/CB SUPPORTED CAMOUFLAGE PAINT WITH HIGH STEALTH TECHNOLOGY TO BE USED IN MILITARY LAND VEHICLES

MELEK ALTAY

M.Sc.

ADANA 2024

TÜRKİYE CUMHURİYETİ
ADANA ALPARSLAN TÜRKEŞ SCIENCE AND TECHNOLOGY UNIVERSITY

GRADUATE SCHOOL
NANO TECHNOLOGY AND ENGINEERING SCIENCES DEPARTMENT

INVESTIGATION OF ADVANCED RADAR ABSORBING PANI/YIG/CB SUPPORTED CAMOUFLAGE PAINT WITH HIGH STEALTH TECHNOLOGY TO BE USED IN MILITARY LAND VEHICLES

MELEK ALTAY

M.Sc.

THESIS ADVISOR
ASSOC. PROF. DR. MUSTAFA AKYOL

ADANA, 2024

DECLARATION OF CONFORMITY

In this thesis study, which was prepared following the thesis writing rules of Adana Alparslan Türkeş Science and Technology University Institute of Graduate School, I declare that I provide all the information, documents, evaluations and results in accordance with scientific ethics and moral codes without resorting to any means or assistance that would be contrary to scientific ethics and traditions. I also declare that I refer to all of the articles I used in this study with appropriate references and accept all moral and legal consequences if a situation is found contrary to my statement regarding my work.

23/01/2024

[Signature]

Melek ALTAY

ÖZET

ASKERİ KARA ARAÇLARINDA KULLANILACAK YÜKSEK GİZLİLİK TEKNOLOJİSİNE SAHİP GELİŞMİŞ RADAR SOĞURUCU PANI/YIG/CB DESTEKLİ KAMUFLAJ BOYASININ İNCELENMESİ

Melek ALTAY
Yüksek Lisans, Nano Teknoloji ve Mühendislik BilimleriAnabilim Dalı
Danışman: Doç. Dr. Mustafa AKYOL
Ocak 2024, 59 sayfa

Gizlilik teknolojisi son yıllarda yoğun olarak çalışılan bir tür savunma teknolojisidir. Buradaki amaç hedef nesnenin radar kesit alanını (RCS) azaltarak radar görünürlüğünü engellemektir. Radar görünürlüğünü azaltmak için ya nesnenin geometrisi ile gelen elektromanyetik (EM) dalganın saçtırma ya da nesnede kullanılan malzemenin EM dalgaları soğurma özelliğine sahip olması gerekmektedir. Radar soğurucu malzemeler, dielektrik ve/veya manyetik kayıp mekanizması ile malzeme içerisine giren EM dalgaların enerjisini azaltarak hedef nesnenin radar görünürlüğünü azaltmaya çalışırlar.

Bu tez çalışması kapsamında, radar soğurucu malzemeler üzerine kapsamlı bir çalışma gerçekleştirilmiştir. Mikrodalga soğurucu bir malzeme olan $Y_3Fe_5O_{12}$ (kısa adı YIG) manyetik tozlar sol-jel yöntemi kullanılarak sentezlendi. Burada farklı ısıl işlem süreçleri uygulanarak yapı içerisinde ara yüzeyler oluşturuldu ve EM dalga soğurma karakteristikleri incelendi. Daha sonra, YIG ve karbon siyahı (CB) malzemeleri ile YIG_{1-x}/CB_x ($0{,}00 \leq x \leq 1{,}00$, 0,25 artışla) kompozitleri katıhal rekaisyon yöntemi ile üretildi. Üretilen kompozitlerin kristal yapıları, manyetik özellikleri ve EM dalga soğurma karakteristikleri incelendi. Son olarak bu kompozitlerin yüzeyleri iletken polimer olan polianilin ile yerinde polimerizasyon yöntemi ile kaplanarak PANI@YIG_{1-x}/CB_x ($0{,}00 \leq x \leq 1{,}00$, 0,25 artışla) hibrit kompozitleri sentezlendi. Hibrit kompozitlerin mikrodalga soğurma performanslarının tatmin edici düzeyde olduğu görülerek potansiyel askeri kara uygulamalarında kullanılabileceği görülmüştür.

Anahtar Kelimeler: Elektromanyetik dalga soğurma, hibrit kompozit, karbon siyahı, radar soğurucu, YIG.

ABSTRACT

INVESTIGATION OF ADVANCED RADAR ABSORBING PANI/YIG/CB SUPPORTED CAMOUFLAGE PAINT WITH HIGH STEALTH TECHNOLOGY TO BE USED IN MILITARY LAND VEHICLES

Melek ALTAY

M.Sc., Department of Nano Technology and Engineering Sciences

Supervisor: Assoc. Prof. Dr. Mustafa AKYOL

January 2024, 59 pages

Recently, stealth technology, which is a type of defense technology, has been studied intensively. The stealth technology aims to prevent radar visibility by reducing the radar cross section (RCS) of target object. To reduce radar visibility, the geometry of the object must either scatter the incoming electromagnetic (EM) wave or the material used in the object must have the ability to absorb EM waves. Radar absorbing materials try to decrease radar visibility of the target object by reducing the energy of EM waves entering the material through a dielectric and/or magnetic loss mechanism.

Within the scope of this thesis, a comprehensive study on radar absorbing materials was carried out. $Y_3Fe_5O_{12}$ (short name YIG) magnetic powders, a microwave absorbing material, were synthesized using the sol-gel method. Here, interfaces were created within the structure by applying different heat treatment processes and EM wave absorption characteristics were examined. Then, YIG_{1-x}/CB_x ($0.00 \leq x \leq 1.00$, 0.25 increment) composites with YIG and carbon black (CB) materials were produced via solid state reaction method. The structural and magnetic properties and EM wave absorption characteristics of the produced composites were examined. Finally, PANI@YIG_{1-x}/CB_x ($0.00 \leq x \leq 1.00$, 0.25 increment) hybrid composites were synthesized by coating the surfaces of these composites with the conductive polymer polyaniline by in-situ polymerization method. The microwave absorption performances of hybrid composites are at a satisfactory level and can be used in potential military land applications.

Keywords: Electromagnetic wave absorption, hybrid composite, carbon black, radar absorber, YIG.

Dedication

(This section is not required to be included in the thesis. If included, the name of the person or institution you want the thesis to be dedicated to is written. e.g., to my precious family)

(Only written text should be used in this section. No symbols or emojis are used. Delete this page if it is not included in the thesis.)

ACKNOWLEDGEMENTS

First of all, I would like to thank and express my gratitude to everyone who has been with me in my thesis studies since my master's degree, who has never spared their support, and who has contributed to my scientific, social and life experiences.

I would like to thank my supervisor, Assoc. Prof. Dr. Mustafa AKYOL, who I had the opportunity to know throughout my undergraduate education, who guided and motivated me with his knowledge and experience throughout my graduate education and who never lost hope in me. He was my biggest supporter with his compassion, interest, patience and teaching whenever I gave up, both at work and during my graduate studies. I overcame many problems with his efforts. He has always been and will continue to be a light in every aspect of my life with his investigative spirit, forward-thinking, assertiveness, educational personality, helpfulness, compassion and honesty.

I would like to express my gratitude to Koluman Automotive Industry R&D Military Projects team, where I worked throughout my thesis process, and for their financially and moral contributions to my thesis with the Radar System in Land Vehicles project.

Finally, I would like to express my sincere gratitude to my family, who is always by my side under all circumstances, supports me financially and morally, and always makes me feel good. I believe that I will achieve everything in life with their support.

This thesis was supported by Adana Alparslan Türkeş Science and Technology University Scientific Research Council with project number 22303007.
This thesis was also partially supported by Koluman Automotive Industry with project number RD57.

TABLE OF CONTENTS

LIST OF FIGURES

LIST OF TABLES

LIST OF ABBREVIATIONS

α	: Attenuation constant
$\vec{B}$	: Magnetic field
C_0	: Eddy current loss
°C	: Celsius degree
D	: Crystallite size
$\vec{E}$	: Electric field
e^-	: Electron charge
EDS	: Energy-Dispersive X-Ray Spectroscopy
GHz	: Gigahertz
g	: Gram
hkl	: Miller indices
$\vec{H}$	: External magnetic field
H_c	: Coercive field
K	: Kelvin
MHz	: Megahertz
m	: Mass
$\vec{M}$	: Magnetization vector
M_s	: Saturation Magnetization
M_r	: Remanence Magnetization
Oe	: Oersted
PPMS	: Physical Properties Measurement System
RAC	: Radar Absorbing Composites
RAM	: Radar Absorbing Materials
RCS	: Radar Cross Section
RL	: Reflection Loss
RF	: Radio Frequency
SEM	: Scanning Electron Microscopy
T	: Temperature
VSM	: Vibrating Sample Magnetometer
XRD	: X-Ray Diffraction

LIST OF SYMBOLS

ε	: Permittivity
μ	: Permeability
Q	: Temperature constant
τ	: Relaxation time
V	: Speed
χ	: Magnetic susceptibility
λ	: Wavelength
θ	: Bragg angle
μ	: Magnetic moment
μ_B	: Bohr magnetron
μ_0	: Free space magnetic permeability
γ	: Gyromagnetic ratio
π	: Pi number

1. INTRODUCTION

Stealth technology, also called low observable technology, can be defined as identifying stationary or moving objects to be less visible (ideally invisible) to satellites, infrared, sonar and other detection methods. Invisibility technology can be applied to a person, but also to a vehicle, rocket, missile or submarine.

The word “radar” is an acronym derived from the phrase Radio Detection And Ranging. The basic principle of radar can be explained by extremely short bursts of radio energy that are transmitted from transmitter. When the transmistted wave reactes with the object and reflected from the target, the returned wave can be collected by a receiver. It utilizes its own radio energy to detect and track the target [1]. Radar is a remote sensing system that transmits an electromagnetic wave (EMW) to the objects and then collects the reflected EMW after EMW communicated with an object (moving or stationary). In addition to detecting the altitude, orientation and speed of objects with radars, objects can also be focused and tracked. In this regard, the radar , in principle, can operate at any microwave frequency. However, in practice, the devices we define as radar are limited to a relatively narrow band of the electromagnetic spectrum due to their component availability, propagation effects, angular resolution requirement, target scattering characteristics, and a number of other concerns. While defense systems are strengthened with surveillance and tracking radars, imaging and remote sensing radars are widely used in all kinds of meteorological, geographical or military information collection systems [2].

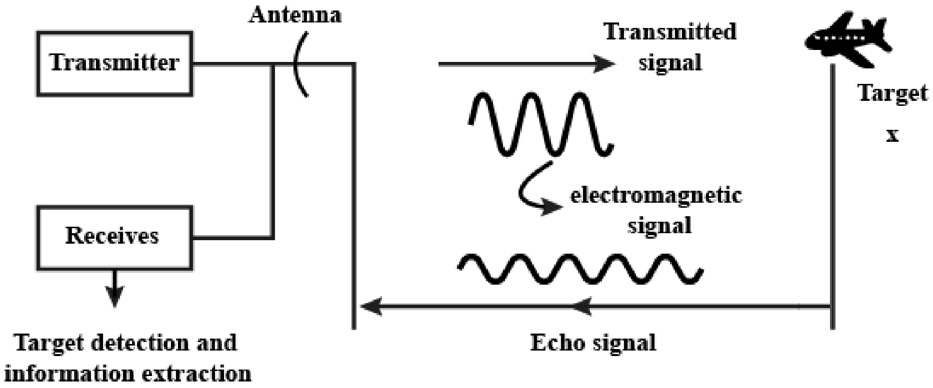

Figure 1.1. The working principle of radar system [3].

Radar bands are divided in various frequency bands for the similarity of propagation effects and target reflectivity. The names, frequency ranges, wavelength ranges and usage areas of these radar bands are given in Table 1.1 that shows the usage areas of each of the bands from 50 MHz to 170 GHz of the electromagnetic wave spectrum. For example, while radio and GPS communications are carried out in the low frequency region, military radar tracking and satellite communications are carried out in the high frequency regions. Therefore, the use of stealth technology depends on whether the object is mobile or not, what its military or civilian mission is, its size, geometry, sound and thermal emission, etc. Range resolution requires large bandwidth [2].

Table 1.1. Microwave frequency bands and their application areas [4].

Band Name	Frequency Range	Wavelength Range	Usage Area
VHF	50-300 MHz	6-1 m	Very long range surveillance, FM radio and television broadcast, radio communication
UHF	300-1000 MHz	1-0.3 m	Very long range surveillance, military communications
L band	1-2 GHz	15–30 cm	Military telemetry, GPS and mobile phones (GSM)
S band	2–4 GHz	7.5–15 cm	Weather radar, surface ship radar, communications satellites, microwave ovens, mobile phones, wireless LAN, Bluetooth, GPS, etc.
C band	4–8 GHz	3.75–7.5 cm	Long-distance radio communication
X band	8–12 GHz	25–37.5 mm	Satellite communications, terrestrial broadband, space communications, missile defense systems,

			naval radar systems, short-range detection
Ku band	12–18 GHz	16.7–25 mm	Radar and satellite communications, high resolution mapping.
K band	18–26.5 GHz	11.3–16.7 mm	Satellite communications
Ka band	26.5–40 GHz	5.0–11.3 mm	Radar and satellite communications, airport surveillance system, very high resolution mapping.
Q band	33–50 GHz	6.0–9.0 mm	Satellite communications, terrestrial microwave communications, radio astronomy and automotive radar.
V band	50–75 GHz	4.0–6.0 mm	Millimeter wave radar research and other types of scientific research.
W band	75–110 GHz	2.7–4.0 mm	Satellite communications, millimeter wave radar research, military radar targeting and tracking applications
F band	90–140 GHz	2.1–3.3 mm	SHF transmissions: radio astronomy, microwave devices/communications, wireless LAN, most modern radars and communications satellites
D band	110–170 GHz	1.8–2.7 mm	EHF transmissions: radio astronomy, high-frequency microwave radio relay, microwave remote sensing, directed energy weapon

The importance of radar systems in functional operations is increasing depending on the level of survivability. Thanks to the decrease in the visibility of a military vehicle in the battlefield, it ceases to be perceived as a threat. Thus, it will not be exposed to ammunition and the vehicle will be able to perform its functions.

Radars are used in almost all applications in military operations, including air defense, weapon detection, surveillance, reconnaissance and target acquisition. Radar systems can operate at day and night. They have relative immunity to weather conditions, and can even provide over-the-horizon coverage. Therefore, they can provide high-resolution images at all distances, detect, localize and track targets.

1.1 Electromagnetic Wave And Absorption Theory

Electromagnetic waves have two components i) electric and ii) magnetic field as shown in Figure 1.2. The angle between electric and magnetic field is 90 degree, and propogation of the electromagnetic wave is perpendicular to them. The Maxwell’s equations define the solution of electromagnetic waves.

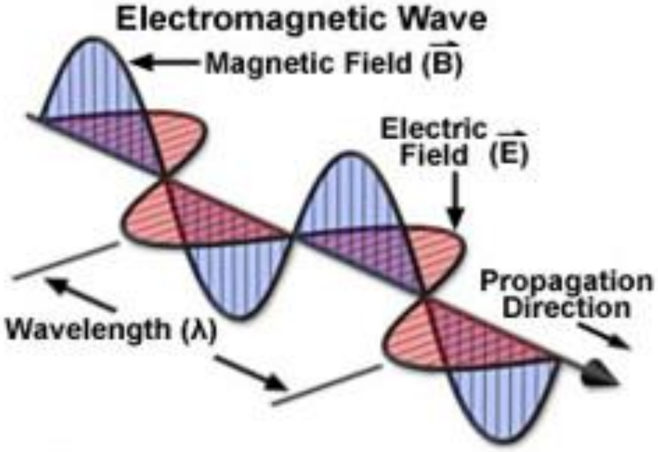

Figure 1.2 Electromagnetic wave [5, 6].

Microwave spectra in the electromagnetic spectrum consists of electromagnetic waves with wavelengths between 1 mm and 1 m, extending from 300 GHz to 300 MHz between infrared radiation and radio frequencies (RF) [7]. The spectrum of electromagnetic radiation, including wavelength ranges for the various colors in the visible spectrum [6]. (Figure 1.2)

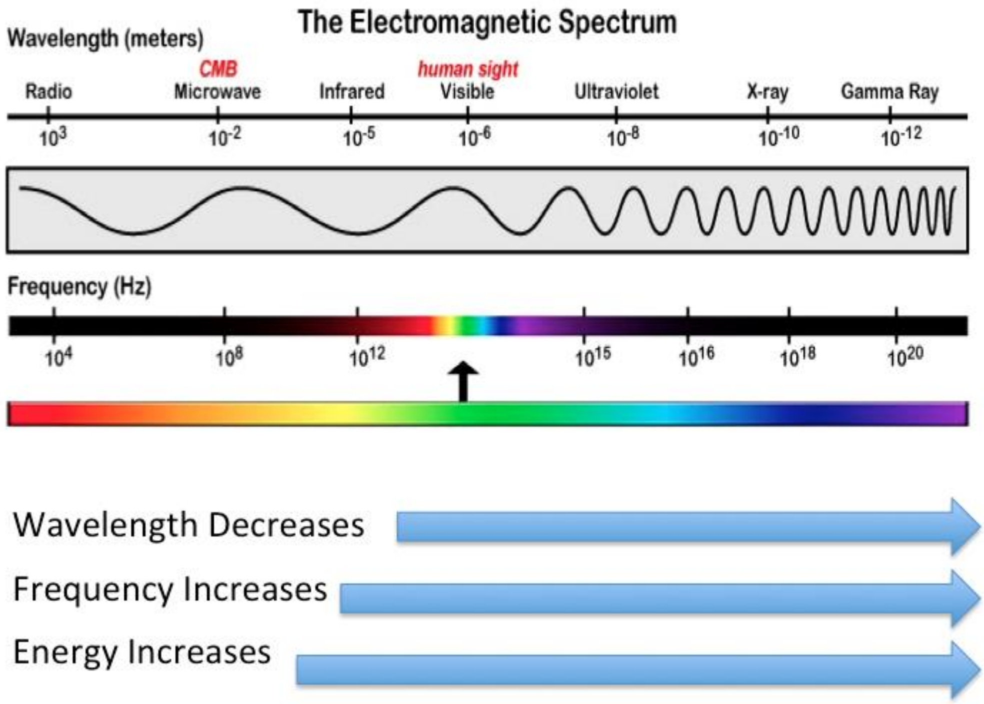

Figure 1.3. Microwave spectrum with increasing frequencies *[8]*.

Electromagnetic methods are used to detect objects of all sizes. In order to understand the functions of electromagnetic waves, it is necessary to know the interaction of waves and objects. The characters of these interactions depend on the materials' physical properties and working frequency.

The propagation of electromagnetic waves are generally defined by permittivity and permeability depending on the frequency [9]. To define it more broadly; the electromagnetic wave characteristic of the material depends on dielectric and magnetic properties of the material.

1.1.1 Dielectric mechanism

Dielectric permittivity ε influences the magnitude of the electric field created by electric charges. The magnitude is inversely proportional to the dielectric permittivity. In free space, the permittivity is constant: $\varepsilon_r = 10^{-9}/36\pi \text{ Fm}^{-1}$. In insulators and polarizable material, the dielectric permittivity increases. The relation between the dielectric of a material and that of free space is given by

$$\varepsilon = \varepsilon_r \varepsilon_0 \qquad (1.1)$$

where ε_r is the relative permittivity or it is commonly known as dielectric constant [10].

1.1.2 Magnetic mechanism

Magnetic permeability (μ) can be defined as the ability of a material to create internal magnetic field under applied magnetic field. Complex magnetic permeability (μ) also consists of real magnetic permeability (μ') defining energy storage and imaginary magnetic permeability (μ'') defining energy loss [7]. Magnetic permeability defined as,

$$\mu = \mu' - \iota\mu'' \qquad (1.2)$$

where μ' and μ'' real and imaginary permeability, respectively.

1.2. Radar Absorbing Structure

The stealth technology can be generally used in defense industry. It is used to decrease radar cross section (RCS) of target object. In addition, it is also used to lose the visibility of the objects in enemy radar systems. RCS is a property of target size, shape and material from which is produced, and it is a ratio of incoming and reflected power [11].

There are two basic methods of implementing privacy technology. The first is to reduce the radar cross-sectional area by dispersing incoming electromagnetic waves by changing the geometry and cross-sectional designs of the vehicle. Another method is to cover certain parts of the vehicle’s surfaces with radar absorbing materials (RAM) that absorb EMWs and lock them into the structure.

The goal of the scientific community is researching and discovering new materials/composites that can decrease electromagnetic radiation levels in order to reduce the detectability of objects by radar.

1.2.1 Shape of military vehicle

Especially in military vehicles, being undetected, is one of the basic elements that increase the level of survivability. In order to prevent the vehicle from being detected, it prevents the reflection of incoming electromagnetic waves by changing the design and shape of its surfaces and corners. Sharp and angled flat surfaces are generally preferred to reduce the echo of electromagnetic waves coming from vehicles.

Most conventional planes have a round shape that makes them aerodynamic and creates a very efficient radar reflector. The round shape means that no matter where the radar signal hits the plane, some of the signal will be reflected back (see Figure 1.4a) [12, 13].

A stealth plane, in contrast, consists of flat surfaces and sharp edges[12]. When a radar signal hits this airplane, it is reflected at an angle as seen in Figure 1.4b [12, 13].

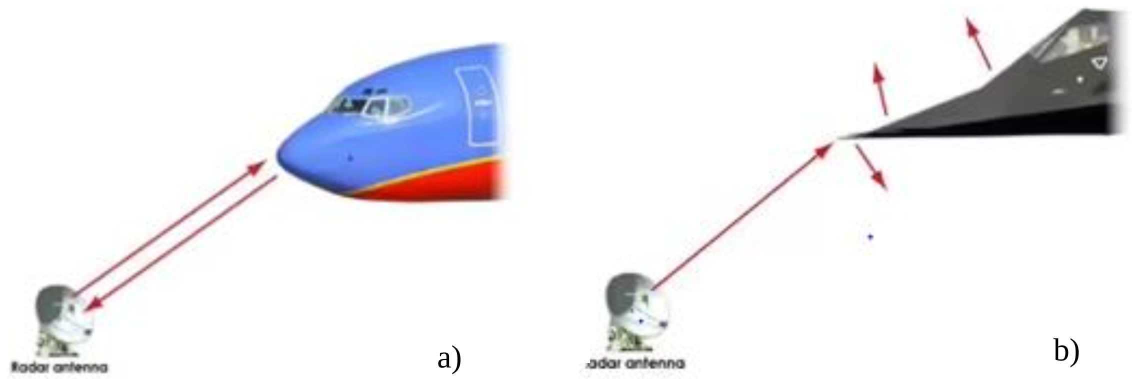

Figure 1.4. The shape of the aircrafts of stealth technology [13].

Stealth technology aircraft is aerodynamically balanced and they achieve high performance and stability through computerized control systems [14]. Vehicle design effects with sharp geometry in stealth technology are also widely used in marine vehicles.

One of the structures that stand out with their special design and shape, which have an active role in stealth technology, is land vehicles. RSC is reduced by using sharp corners on all surfaces in land vehicles.

1.2.2 Radar absorbing materials

Radar Absorbing Materials (RAMs) can absorb electromagnetic energy and convert it into thermal energy[15]. Conventionally, materials such as metals, metal particles, ferrites, conductive polymers and dielectric materials have been used as radiation absorbers. However, aspects such as high density, susceptibility to corrosion, weight or low absorption have limited their application as absorbent materials in practical activities[15]. Ideally, a RAM should be thin, light, and have high electrical conductivity, magnetic susceptibility, high thermal stability, and corrosion resistance [15].

1.2.3 Dielectric absorbers

The most of the polymeric matrices are transparent to microwaves, and absorption, in these materials, occurs due to interactive loss processes of dielectric and magnetic dipoles of the particulates. The complex permittivity;

$$\varepsilon_r{}' - j\varepsilon_r'' \qquad (1.3)$$

in case of dielectric absorber, is an important parameter, which determines the absorption properties of the composite [16]. Materials of this class offer many advantages over ferrite materials because they are light as the main material and therefore do not weigh much in military vehicles [17].

1.2.4 Magnetic absorbers

Ferrites are generally used in magnetic absorbers. There is great interest in soft ferrites as radar absorber materials. Ferrites are ceramic materials. In other words, it shows both very good magnetic and very good mechanical performance at high temperatures up to Curie points [17].

Ferrites are preferred as the best magnetic components for electromagnetic wave absorbing composites due to their high magnetic properties. They are often used in combination with absorbent rubbers, epoxy resins and various paints as absorbent composite structures in various military vehicles.

1.3. Radar Absorbing Camouflage Paint

Camouflage paints on military land vehicles are very important for the survivability of the vehicle. By using camouflage paint on armor steel, which is actively used especially in armored military land vehicles, the ballistic protection of the vehicle is provided and the survivability level in the main battlefield is also increased. The risk of being hit decreases for each vehicle that has a difficulty detecting a target.

It makes a great contribution to privacy for remote physical detection. In order to achieve a similar level of stealth in radar detection, invisibility technology is increased by adding RAM material into camouflage paints.

Figure 1.5. Camouflage paint effects for military vehicle (FMV defence ındustry) *[18]*.

1.4. Armor Steel in Military Vehicles

Various armor materials are used to provide ballistic protection in military land vehicles. The most commonly used material is armor steel, especially when considering suitability for manufacturing, vehicle integration and weight. Armor steel has huge prospective applications in the design of military equipment against the high-speed impact of projectiles due to its high strength, hardness, ductility, etc.[19].

Figure 1.6. Vehicle cabin with ballistic protection provided by armor steel (Koluman, Derman).

1.5. Invisibility in the Microwave Region

Microwaves are defined as electromagnetic radiations with frequencies ranging from 50 MHz to 300 GHz. In contrast, the wavelength varies from 1 mm to approximately 6 m. Microwave radiation is often called microwaves. The bands in the electromagnetic wave spectrum given in Table 1.1 show microwaves and their usage areas.

In the modern warfare scenario, the detection of airborne platforms, i.e. fighter jets, unmanned aerial vehicles (drones), missiles, etc., through advanced ground and air-to-air radar detection is becoming an increasing challenge[20]. Therefore, the demand for "Stealth Technology", which deals with techniques to prevent or delay the detection of airborne objects from all enemy sensors used during tactical operations, is greatly increasing. The main purpose here is to make the enemy unaware of the exact location and presence of defensive equipment. Apart from designing the airframe to reduce the RCS of aircraft/drones, applying functional materials with radar absorption capabilities is the only feasible solution for implementing stealth features. Therefore, the development of new microwave absorber materials (RAM) to meet these requirements has been adopted by the scientific community. The development of RAMs began in the early 1950s with the use of carbon, ferrite and their composites. Advances in structural, microstructural and chemical properties have improved microwave performance, with more than 100 different materials discovered over the past sixty years. Various carbon materials (Carbon Black, Carbon Fibers, Carbon nanotubes, Graphene, conductive polymer, porous carbon), magnetic metals/alloys and their ferrites (e.g. Fe/Ni/Co, FeCo, FeNi, Fe_3O_4, Ni/Zn/Mn/Co, hexaferrites, perovskite oxides), metal oxides ($TMO_{x,}$ TM:Zn, Ti, Al etc), nanomaterials, sulfides, phosphides, 2D MXenes and high-entropy alloys are being investigated for EMW absorption in microwave region of the spectrum. Microwave absorption property can be enhanced by the morphological effect of nanomaterials from 0D nanoparticles to 1D (nanofibers, nanowires), from 2D-nanosheets (layered, hexagonal platelet, nanoflakes) to 3D – (hierarchical, flower-like, quadrupeds, web-like structures).

Figure 1.6 shows the change over the years of the research results obtained by entering Scopus keywords carbon, magnetic metals and metal alloys, ferrites, sulphides, phosphides, carbides, MXenes, high entropy alloys and microwave absorber materials together. It can be seen from Figure 1.1 that the number of research articles shows an increasing trend every year. A large number of materials have been investigated for microwave absorption applications since the 1950s, and the search for efficient materials continues. The electromagnetic absorption performances of composite materials created with each material and/or material group have also been intensively researched in recent years. However, due to the difficulty and high costs of the production processes of almost all the materials mentioned here, they are generally applied to strategically important defense vehicles (such as warplanes, unmanned aerial vehicles).

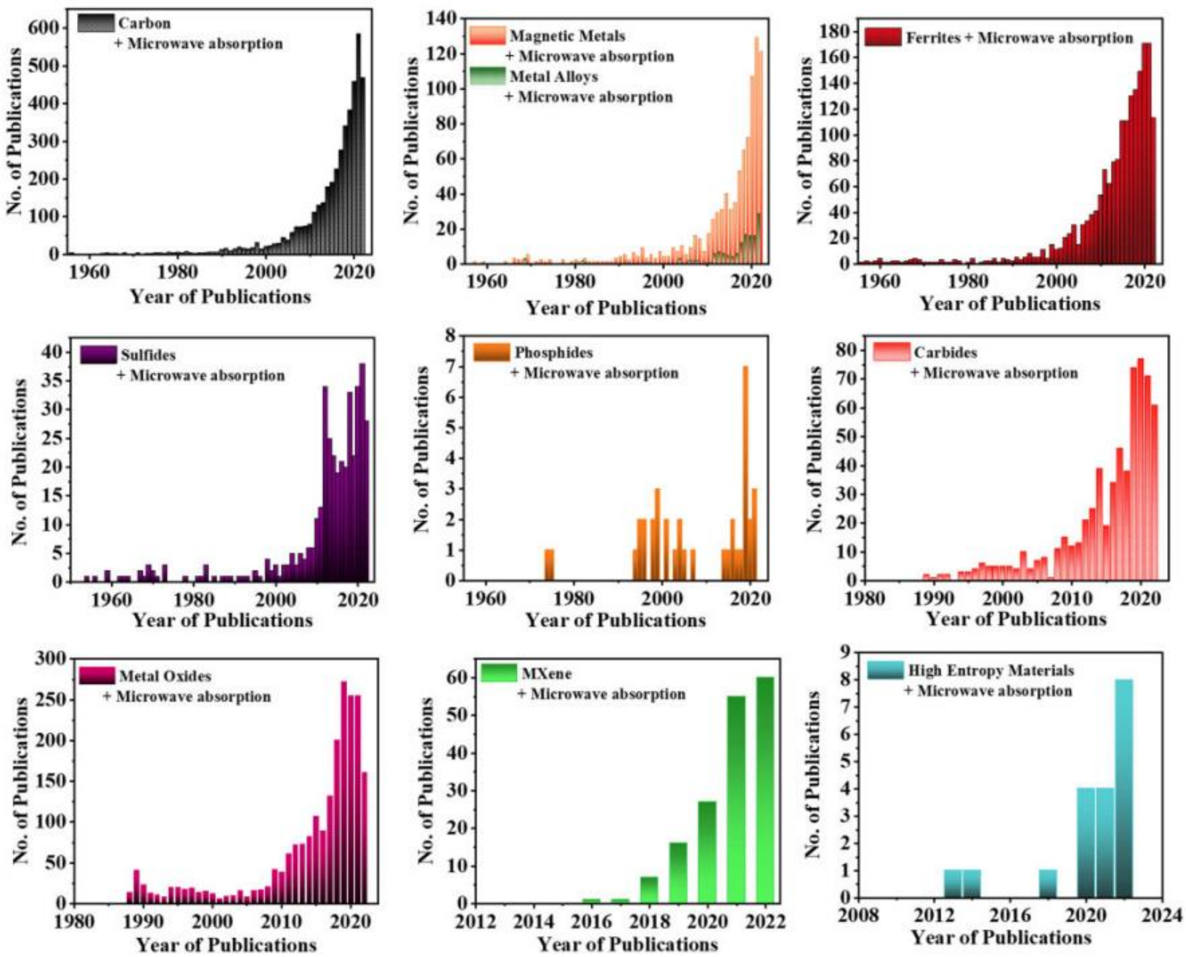

Figure 1.7. Histograms showing the number of publications and year of publication for carbon, magnetic metals and metal alloys, ferrites, sulphides, phosphides, carbides, metal oxides, MXenes and high-entropy materials and RAMs searched as keywords from Scopus [20].

Figure 1.7 shows the change over the years of the research results obtained by entering Scopus keywords YIG and microwave absoprtion together. It can be seen from Figure 1.7 that the number of research articles becomes almost constant in between 1960 and 2014. After that the number of publication increases with the year and finally reaches its maximum level in 2023. On the other hand, when we search the Scopus by giving YIG and carbon, there is no any result occuring. In this thesis, polyaniline coated YIG_x/CB_{1-x} (x:0.00, 0.25, 0.50, 0.75 and 1.00) composites were synthesized and their structural, magnetic and electromagnetic wave absorbing performance were studied in detail to fill the blank in the literature.

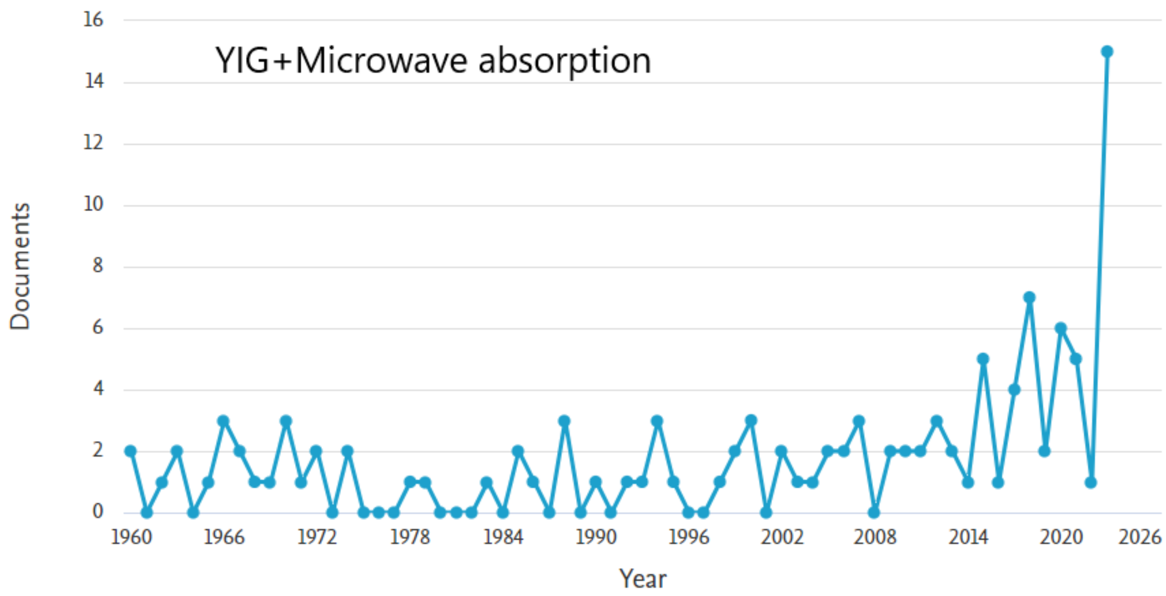

Figure 1.8. The number of publications and year of publication for YIG and RAMs searched as keywords from Scopus.

2. LITERATURE REVIEW

In this part of the thesis, studies on the production and characterization of various radar absorbing materials and composites and the use of camouflage paint with ram materials are discussed. We will present a brief summary of the studies in the literature on radar absorber systems and their use with armor steels.

Ting T.-H. et al (2010) were synthesized polyaniline/$BaFe_{12}O_{19}$ (PANI/Ba ferrite) composites at different aniline/Ba ferrite weight ratios (Ani/Ba ferrite = 1/2, 1/1 and 2/1). They used as polymerization method to synthesize their composites. They used some spectroscopic characterization methods to study the effect of Ani/Ba ferrite ratio on the physical propertis of composites. The Fourier transform infrared (FTIR), ultraviolet-visible spectrophotometry (UV-Visible), X-ray diffraction (XRD), scanning electron microscopy (SEM), transmission electron microscopy (TEM) were used for characterization. The EMW absorbing properties were investigated by measuring complex dielectrics (permittivity and permeability) in the 2–18 and 18–40 GHz frequency ranges by using the free space method. The results showed that a wider absorption frequency range could be achieved by adding different polyaniline contents into Ba ferrite[21].

Wang M., et al. (2015) were studied conductive polyaniline (PANI) and nickel zinc ferrite binary composites synthesized by in situ polymerization process. To interpret the XRD curves, it was observed that pure ferrite and its composites with different molar ratios had diffraction peaks for spinel type crystals. FTIR spectra showed PANI (1562, 1481, 1301, 1109 and 799 cm-1) peaks and NiZn ferrite (579 and 390 cm-1) bonds; this indicated the presence of both NiZn ferrite particles and PANI. Thermogravimetry (TG) curves of pure PANI and composite materials with different molar ratios showed the amount of ferrite in the composite. It was also found that the best electromagnetic absorption feature and wide absorption bandwidth can be obtained with the ratio n(PANI):n(Ni0.6Zn00.4Fe2O4)=1:2. The highest reflection loss of Ni0.6Zn00.4Fe2O4/PANI at 1:2 ratio was obtained as -41 dB at 12.8 GHz, and the bandwidth at -10 dB reached 5 GHz with 2.6 mm absorber thickness [22].

Akyol M. et al (2023) were examined conductive polymer coated $Y_3Fe_5O_{12}$ (YIG)/$NiFe_2O_4$ (NFO) hybrid radar absorber composites. They seynthesized both YIG and NFO magnetic particles via the well-known sol–gel method. After that they covered YIG/NFO composites with conductive polyaniline via in-situ polymerization method. In the structural analysis, they observed both YIG and NFO crystalline peaks in the XRD spectrum. The intensities of these crystalline peaks are consistent with the amount of each component in the composites. Next, they worked on the electromagnetic wave (EMW) absorbing properties of the PANI@YIG/NFO hybrid composites in the 8-12 GHz frequency range. The bandwidth that absorbs EMW in the X-band increases with the YIG content in hybrid composites. Increasing the absorption properties of the composites by the YIG content is explained by a balance between magnetic and dielectric loss in their hybrid composite structures. Therefore, experimental results of hybrid composites may be a promising candidate for radar and defense vehicles due to their fully absorption properties in the X band.[23]

Kıvrak B. et al (2023) were synthesized YIG/CFO ($Y_3Fe_5O_{12}$/$CoFe_2O_4$) hybrid composites covered by conductive PANI. The structural, magnetic and morphology of samples were investigated by various characterization techniques (XRD, VSM, SEM). For the EMW performance of produced composites, they used waveguide technique. They found that the PANI@YIG/CFO hybrid composites had 90% absorption of incoming EMW in the 8-12 GHz frequency range. The minimum reflection loss value was observed as -47 dB with 4 GHz bandwidth that it indicated the whole X-band was absorbed by this kind of hybrid composite.

Aka C. et al (2023) worked on a systematic study which was presented by examining some physical and electromagnetic properties of hybrid nanocomposites. They used magnetic nanoparticle (Fe_3O_4) decorated two dimensional MoS_2 nanosheets as a core and conductive polyaniline as a surface coateding material in hybrid nanoccomposites. They found a broadband electromagnetic wave absorbing properties in Fe_3O_4:MoS_2 and PANI@Fe_3O_4:MoS_2 hybrid nanocomposites. The minimum reflection loss values were found to be -54.97 dB and -39.96 dB in the Fe_3O_4:MoS_2 and PANI@Fe_3O_4:MoS_2 nanocomposites, respectively. Although the RL value was lower in PANI@Fe_3O_4:MoS_2 than that of

$Fe_3O_4:MoS_2$, the effective bandwidth of PANI@$Fe_3O_4:MoS_2$ is wider (7.65 GHz) than the $Fe_3O_4:MoS_2$ nanocomposite. According to the experimental results, PANI@$Fe_3O_4:MoS_2$-like hybrid nanocomposite with light weight and high temperature resistance can absorb almost 90% of incident EMW in a wide bandwidth[24].

3. MATERIALS AND METHODS

Materials can be synthesized by physical and/or chemical methods. Each of them has various types. The chemical methods are commonly used to produce nano/micro-scale materials such as flame synthesis, ultrasonic spray pyrolysis, chemical vapor condensation. Among the chemical methods, the sol-gel method has more advantageous due to its homogenous outputs, low cost and high reproductive rate.

In this section, the preparation procedures of $Y_3Fe_5O_{12}$ (called YIG) particles, YIG_{1-x}/C_x composites and polyaniline (PANI) coated YIG_{1-x}/C_x hybrid radar absorbing composite (RAC) (x=0.00, 0.25, 0.50, 0.75 and 1.00) structures will be explained. In addition to RACs, the RACs were used as a paint for possible land-vehicles applications. The characterization techniques for the investigation of structural, morphological and magnetic properties of YIG, CB and PANI particles and their composites will be given in this section. The electromagnetic wave absorbing performance tests of the produced RACs reinforced epoxy matrices will be also given in detail.

3.1. Sol-Gel Synthesing Process

The sol-gel method is based on the molecular dissolution of the starting inorganic compounds such as metal salts, nitrates, hydroxides and oxides prepared in appropriate stoichiometric ratios in a liquid. In this method, the product with a very homogeneous distribution can be obtained due to the dissolution of chemicals in solution forming on a molecular basis in the liquid. The name sol-gel comes from the abbreviations of the words solution-gelation.

3.2. Synthezing of YIG Particles

Yttrium(III) nitrate hexahydrate-$Y(NO_3).6H_2O$, Iron (III) nitrate nanohydrate-$Fe(NO_3)_3.9H_2O$, citric acid and Ethylene Glycol (EG) were used to produce of $Y_3Fe_5O_{12}$ (YIG) compounds. All chemicals mentioned above were purchased from Sigma-Aldrich company.

$Y_3Fe_5O_{12}$ particles as powder form were synthesized via one-step sol–gel method. Figure 3.1 indicates a schematically illustrated sol-gel method for $Y_3Fe_5O_{12}$ production. The starting [$Y(NO_3).6H_2O$ and $Fe(NO_3)_3.9H_2O$] salts were suspended in 15 ml of distilled water (DI-water) and stirred for 30 minutes. Citric acid suspended in DI-water in another beaker was added into the mixture of Y and Fe solutions. The mixture was stirred another 30 minutes at 70 °C. After this point, ethylene glycol was injected into the final solution on the magnetic stirrer. To make a gel form, the solution beaker was heated at 250°C. After that gel-formed sample was kept into high temperature oven at 500 °C for 1h. The powder form of sample was ground in an agate mortar for 15 min. Then, the fine powders were further calcinated at 550 °C for 5 h. The calcinated powders were pressed to make pellets in a cylindrical form (10 mm diameter) under 20 bar pressure. Finally, the sintering process was performed at various temperatures 700°C, 800°C, 900°C, 1000°C and 1100°C for 24 hours. The corresponding samples are called as YF700, YF800, YF900, YF1000 and YF1100 [25].

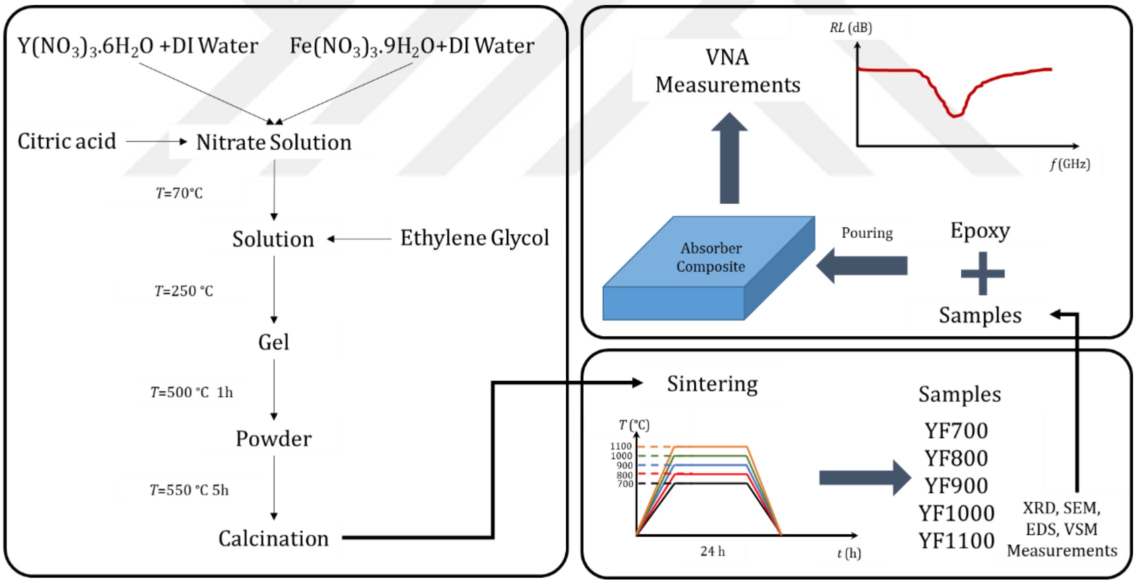

Figure 3.1. Sol-gel process for the synthesis of $Y_3Fe_5O_{12}$ powders.

The synthesized powders (YF700, YF800, YF900, YF1000 and YF1100) as explained above are splintered in epoxy resin to make a composite for X-band EMW measurement. The particle and epoxy resin weight ratio were used as 70% and 30%, respectively. The magnetic particles and epoxy resin were mixed for 30 min to provide homogeneity. Then, the curing agent was added to the mixture. In addition, the mixture was left in the vacuum chamber to prevent the formation of gas bubbles. Finally, the mixture was cast into a 22.86×10.16×4.00 mm^3 rectangular silicone mold for the X-band electromagnetic measurements. The material epoxy/hardener mixture in the silicone mold was left at room temperature for one day. After curing was completed, the cured composites were removed heedfully from the silicon mold.

3.3. Production of YIG_{1-x}/CB_x Composites

The YIG_{1-x}/CB_x (x=0.00, 0.25, 0.50, 0.75 and 1.00) composites were produced by solid-state-reaction method. The carbon black powders were directly added to the YIG powders in desired amounts to create various form of YIG/CB composites.

Table 3.1. Sample codes and the contents of YIG_{1-x}/CB_x composites.

Sample Code	Powder Content (%)	
	YIG	CB
YC1	100	-
YC2	75	25
YC3	50	50
YC4	25	75
YC5	-	100

3.4. Polyaniline Coating of YIG_{1-x}/CB_x Composites

As a conductive polymer, polyaniline was coated of YIG_{1-x}/CB_x (x=0.00, 0.25, 0.50, 0.75 and 1.00) composites by in-situ oxidative polymerization method. In this method, first of all, the appropriate amount of YIG/CB powders were weight by a scale and then they were dispersed in a HCl solution. In a meanwhile, the ammonium persulfate (APS) and aniline solutions were prepared in two different beakers under ice bath. The temperature of the bath was kept under 5 °C during the polymerization process. The APS solution was added into the aniline solution drop-by-drop. The residual solution was washed with distilled water and ethanole in three times. The washed and cleaned YIG_{1-x}/CB_x samples were dried in oven at 70 °C for 24 h. The produced sample codes and their contents are tabulated in Table 3.2.

Table 3.2. Sample codes and the contents of PANI@YIG_{1-x}/CB_x hybrid composites.

Sample Code	Polymer (%)	Powder Content (%)	
	PANI	YIG	C
PYC1	50.0	50.0	-
PYC2	50.0	37.5	12.5
PYC3	50.0	25.0	25.0
PYC4	50.0	12.5	37.5
PYC5	50.0	-	50.0

3.5. Characterization Techniques

The structural properties of the synthesized powders were investigated by x-ray diffractometry (XRD) with Cu-Ka radiation. Surface morphology of synthesized powder samples were investigated by scanning electron microscopy (SEM). The elemental analysis were performed by using energy distribution X-ray spectrometry (EDS) which is integrated in the SEM system. The magnetic characteristics of the powder samples and their composites were studied by vibrating sample magnetometer (VSM) at room temperature. The electromagnetic wave absorbing performance of the composites were investigated by vector network analyzer (VNA). In the following section, we will describe each characterization techniques.

3.5.1. Structural analysis

3.5.1.1. X-ray diffraction (XRD) method

The diffraction mechanism in crystalline structure was discovered by German physicist Max von Laue. When the atoms of a material were in crystal form, x-rays were refracted in characteristic angles. The conditions required for diffraction can be expressed in a simple mathematics relation called "Bragg's Law". In order to explain the Bragg law, the reflection of x-rays from two adjacent planes with a distance d between them is shown in Figure 3.2.

$$n\lambda = 2dsin\theta \qquad (3.1)$$

where λ is the wavelength of the x-ray, the θ is angle between the incident light and the reflection plane, d is the distance between the planes and n is an integer. Bragg reflection occurs only if it satisfies the condition $\lambda \leq 2d$. This result also gives a physical explanation on why we cannot use visible rays.

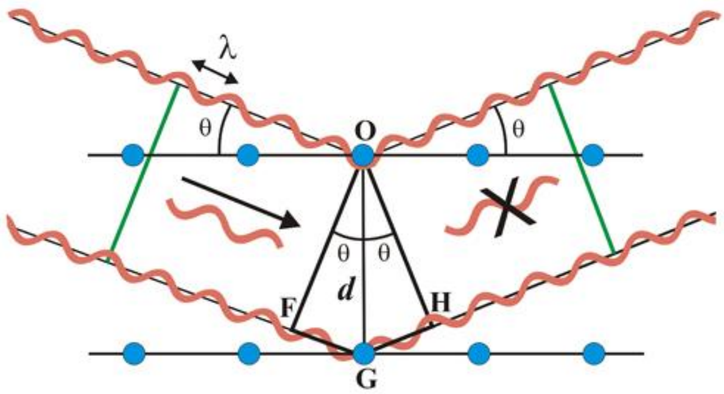

Figure 3.2. X-ray diffraction and Bragg's law on crystal planes [26].

In the powder diffraction method, the crystal to be examined is turned into very fine powder and placed in a monochromatic (single wavelength) x-ray beam. Each part of the powder crystal is a very small crystal that is arbitrarily oriented relative to the incoming bundle. The maximum reflection occurs when the x-ray is oriented with the crystal planes to make the correct Bragg angle, and the scattered x-rays reach the monochromator and then the detector through the router slit. X-ray diffraction pattern is shown in a graph of the diffracted beams intensity as a function of the reflection angle (2θ). XRD measurements of the samples in this study were performed by using Rigaku Miniflex x-ray diffraction analysis system (see Figure 3.3) with Cu-Kα (1.5405 Å) x-ray source in the our x-rays laboratory. Measurements were carried out at room temperature between 5° and 90° in steps of 0.02°.

Figure 3.3. Rigaku Miniflex x-ray diffractometer.

3.5.1.2. Scanning electron microscopy (SEM) and energy-dispersive x-ray spectrum (EDS) methods

Scanning electron microscopy (SEM) is used to observe the morphology of the materials in high resolution. Since SEM takes pictures from the surface of the material, the accelerated high energy electrons are scaned through the selected surface of the materials. Typically, the electron beam produced by heating a metallic filament such as tungsten leaves the gun and passes through the electromagnetic lenses which focus the beam. When these electron beams hit materials, they interact with the materials' atoms (elastic and inelastic collisions) and cause scattering of other electrons from the material. The scattered electrons are collected from each pixel of a detector to create a suitable point-to-point image. Therefore, an image of the scanned material can be obtained.

Energy-dispersive x-ray spectroscopy (EDS) is an elemental analysis method. It determines the elements and their quantities in a material. The x-rays emitted from the material surface exposed to high energy electron beam show characteristic features due to their energy and wavelengths. These characteristic x-rays are detected by special x-ray detectors. Thanks to the peaks obtained from the characteristic x-ray energy values of the elements, the analysis of the elements in the material is performed.

SEM images and EDS analyzes of the polycrystalline samples produced within the scope of the thesis were taken using the EDS integrated FEI Quanta FEG 650 model scanning electron microscope in the Çukurova University Central Research Laboratory (Figure 3.4). Tabletshaped materials were cleaned and placed in the sample holder and SEM images were taken at at various magnification rates under vacuum. EDS analyzes were performed at 20 kV acceleration voltage.

Figure 3.4. FEI Quanta FEG-650 type scanning electron microscope with EDS integrated.

3.5.2. Magnetic analysis

The Physical Property Measurement System (Quantum Design, PPMS) is a highly integrated system designed as the primary research equipment to accurately measure the physical properties of the material. PPMS system includes a variety of module in a one system. One of these modules is vibrating sample magnetometer (VSM). The PPMS systems are actively used in research laboratories worldwide and have the highest sensing sensitivities at wide temperature and magnetic field values required for material characterization. Temperature control system is sensitive to work between 2 K (-271ºC) - 400K (127 ºC) temperature range and provides control of heat flow to the sample area. The magnet control system adjusts the current from the power supply to create ±9 T magnetic field and allows the user to work in both continuous and discontinuous modes.

Magnetic measurements of all samples in this study were made using the Physical Property Measurement System (Quantum Design) PPMS Dyna Cool in ÇÜMERLAB laboratories (Figure 3.5). The operating temperature range of the system is 2-400 K and measurements can be taken at ± 9T magnetic field values. The magnetic hysteresis measurements were made at 300 K temperature for all samples.

Figure 3.5. Quantum Design Dyna-Cool model Phyical Property Measurement Sytem (PPMS).

3.5.3. Electromagnetic analysis

Network analyzer is an important system for the analysis, control and monitoring of components and devices to be used in microwave (RF) systems. Network analyzer provides to measure of network scattering parameters, reflection measurements and analysis of S parameters of samples. The electromagnetic properties of the RAC samples specified in Table 3.1 were studied in the frequency range of 8 GHz-12 GHz, called as X band. Composite samples for reflection loss measurements are manufactured in standard waveguide size of X-band as 22.86 mm (0.9 inch) long and 10.16 mm (0.4 inch) wide. In order to provide full reflection in the analysis part, aluminum sheet having 1 mm thickness is integrated back to the samples in composite production. Thus, the reflection of the electromagnetic waves passing through the sample is provided and it is provided to pass through the composite sample again. The purpose here is to calculate the energy loss at the entrance and exit of the wave and the absorption capacity of the structure. In the thesis study, all of the electromagnetic analysis of composite samples were made by the KEYSIGHT PNA-L Network Analyzer system in İskenderun Technical University (Figure 3.6). Reflection loss graphs in the range of 8 GHz and 12 GHz frequencies were obtained in dB.

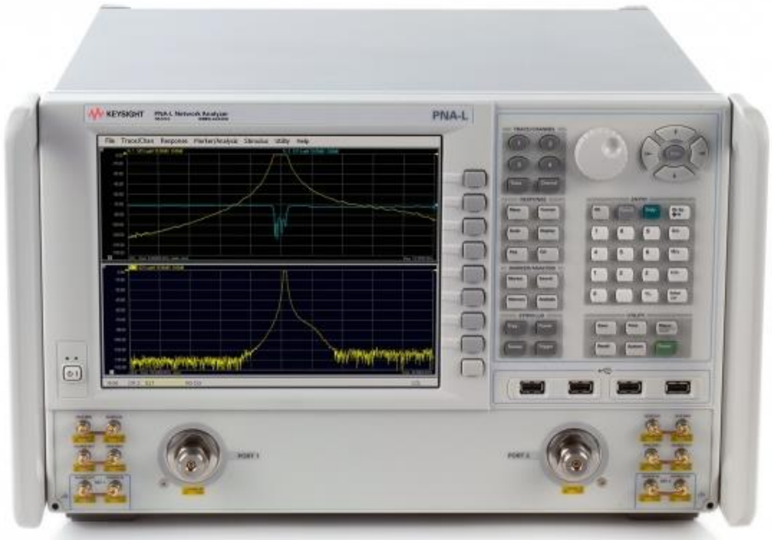

Figure 3.6. PNA-L type KEYSIGHT network analyzer system.

4. RESULTS AND DISCUSSIONS

In this thesis, $Y_3Fe_5O_{12}$ (YIG) magnetic powders were first synthesized by sol-gel method as explained in Section 3.1. The YIG_{1-x}/CB_x (x=0.00, 0.25, 0.50, 0.75 and 1.00) and PANI@YIG_{1-x}/CB_x radar absorbing composites (RACs) were produced for electromagnetic wave absorbing performance as explained in Chapter 3. Structural, magnetic and electromagnetic characterizations of YIG samples sintered at various temperature are discussed in Section 4.1. The structural, magnetic and electromagnetic wave absorbing performance of YIG_{1-x}/CB_x (x=0.00, 0.25, 0.50, 0.75 and 1.00) composites and PANI@YIG_{1-x}/CB_x hybrid composites are discussed in Section 4.2 and Section 4.3, respectively.

4.1. Sintering Temperature Effect on the Structure, Magnetic and Electromagnetic Characteristic of YIG Particles

Here, the amount of interface in $Y_3Fe_5O_{12}/Fe_2O_3$ composite was investigated by measuring EMW parameters. The multi-crystal phases formation was obtained by performing one-step heat treatment process. Because the interface effect in between $Y_3Fe_5O_{12}$ and Fe_2O_3 crystals is lack in the literature, a systematic study has been carried out in this thesis.

4.1.1. Structural properties of YIG particles

Structural properties of YIG particles were studied by measuring x-ray diffraction in between 20º≤ 2θ ≤80º. Figure 4.1a indicates XRD patterns of synthesized materials. The XRD data were further analyzed by X-Pert High Score software. As a result of the analyses, multi-crystal formations Fe_2O_3 (*) and $YFeO_3$ (•) and $Y_3Fe_5O_{12}$ have been detected in the samples. The each crystal amounts have been calculated and shown in Figure 4.1b. One is observed that when sintering temperature increases from 700 to 1100°C, the $Y_3Fe_5O_{12}$ crystal phase amount increases and becomes dominant in the whole structure. The YIG structure displayed crystalline peaks at 28.8°, 32.3°, 35.5°, 39.9°, 45.1°, 51.1°, 53.2°, 55.5°, 59.6°, 67.5°, 69.4°, and 71.2° with diffraction planes of (400), (420), (422), (521), (611), (444), (640), (642), (800), (840), (842), and (664), respectively [25]. These peaks correspond to the cubic crystal structure of YIG with *Ia-3d* space group symmetry, in agreement with JCPDS standard data (Card No. 01-077-1998). The YIG crystallite size of the samples were calculated by using the basic Scherrer equation [27].

$$D = \frac{K\lambda}{\beta cos\theta} \tag{4.1}$$

where D is the crystallite size, λ is the x-ray wavelength (CuKa = 1.5406 A °), β is the width of the x-ray peak on the 2θ axis measured as full width at half maximum (FWHM), θ is the Bragg angle, K is the so-called Scherrer constant. K is used as 0.9 in this thesis [28].

Table 4.1. Sample codes and their corresponding chemical formulas for optimization of sintering temperature samples.

Sample Code	Temperature (°C)	Crysytal Content (%)		
	T	YIG	$YFeO_3$	Fe_2O_3
YF700	700	-	46	54
YF800	800	-	47	53
YF900	900	43	26	31
YF1000	1000	69	5	26
YF1100	1100	88	1	11

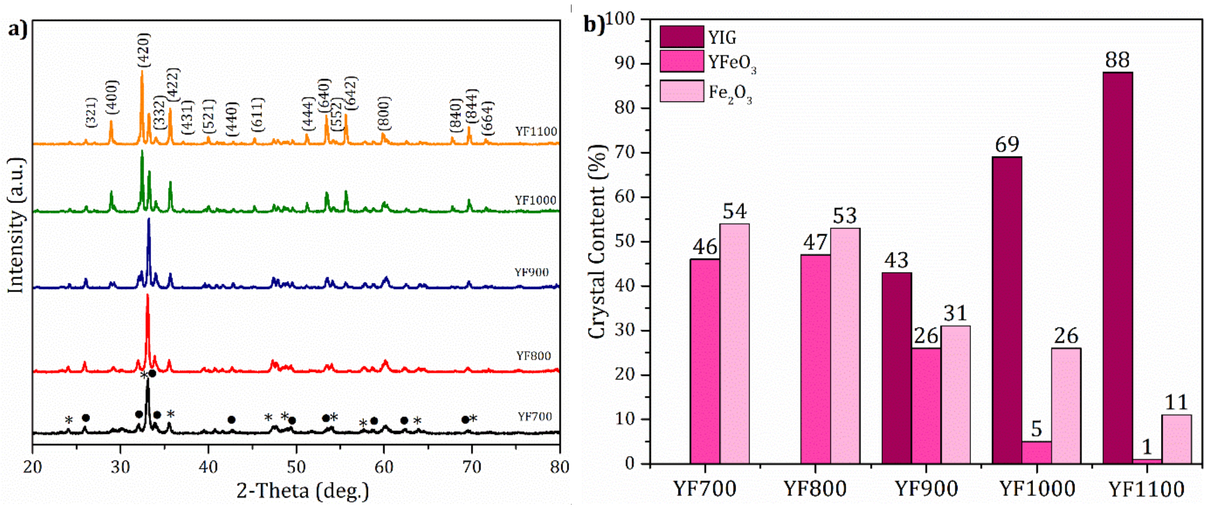

Figure 4.1.a) X-ray diffraction patterns and **b)** the amount of $Y_3Fe_5O_{12}$, $YFeO_3$ and Fe_2O_3 crystals in the samples.

4.1.2. Morphological properties of YIG particles

Surface morphologies of YF700, YF800, YF900, YF1000 and YF1100 materials were observed by taking SEM images (see Figure 4.2(a-e)). In YF700 and YF800 samples, the grain boundaries were not detectable and their sizes were small when they compared to other samples (Figure 4.2(a-b)). The grains and their boundaries can be easily observed in sample sintered at 1000ºC. In addition, the grain size is increased in YF1000 sample when it compared to other samples. However, above 1000ºC, the grain boundaries cannot be easily detectable because of the melting (see Figure 4.2e). The average grain size (AGS) of YF900, YF1000 and YF1100 materials are determined by randomly selected 100 grains from SEM images. AGS values were found as 201nm, 375nm and 309nm for YF900, YF1000 and YF1100, respectively. EDS spectrum for YF1000 material was carried out to identify the elemental analysis. Figure 4.2f shows the presence of all expected elements (Y, Fe and O) without impurities. The atomic/weight percent of the detected elements are tabulated as an inset in Figure 4.2f. The chemical composition of YF1000 sample is confirmed by EDS [25].

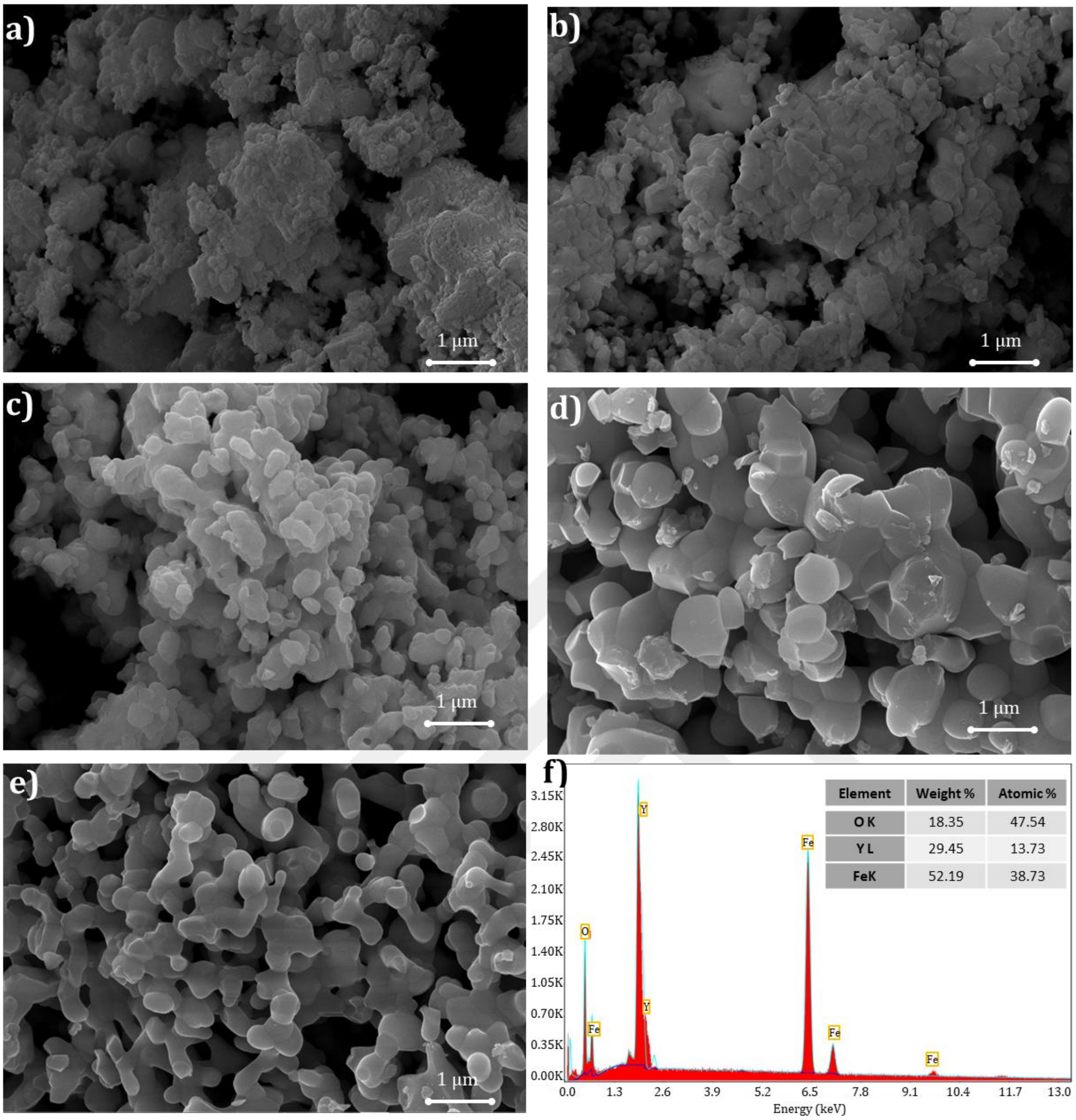

Figure 4.2.a-e) Scanning electron micrographes of materials. **f)** EDS graph of YF1000 sample.

4.1.3. Magnetic properties of YIG particles

The magnetic hysteresis (*M-H*) loops of the YIG samples sintered at various temperatures are shown in Figure 4.3a. The *M-H* loops measurements were performed at 300K under ±3T magnetic field. Weak magnetization values have been observed in YF700 and YF800 samples (see inset of Figure 4.3a). Once the sintering temperature is reached 900ºC, the magnetization values of the YF900 sample are enhanced because of increasing the amount of $Y_3Fe_5O_{12}$ crystal. A soft ferromagnetic hysteresis curves are observed in YF1000 and YF1100 samples. Two important parameters for magnetic materials have been determined by using hysteresis curves. These are saturation (M_s) and remenant magnetization (M_r). Both M_s and M_r values of the produced samples increase with the increase of sintering temperature (see Figure 4.3b). As expected the highest M_s value is determined in YF1100 as 20.2 emu/g because of its highest YIG content. The M_s value of YF1100 samples is consistent with some studies [29, 30]. A correlation between structural and magnetic properties in YIG/Fe_2O_3 samples have been observed [25].

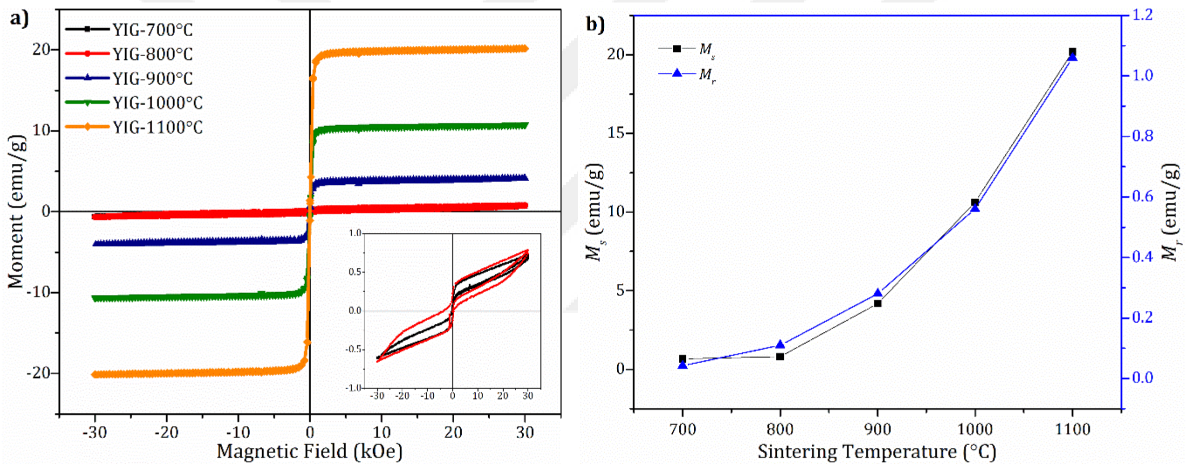

Figure 4.3.a) *M-H* loops and **b)** M_s, M_r values of $Y_3Fe_5O_{12}/Fe_2O_3$ samples.

4.1.4. Electromagnetic wave absorbing properties of YIG particles

The samples' electromagnetic wave absorbing performance were investigated in between 8 and 12 GHz frequency range. As explained in Section 3.5.3, the samples (30%) were cured in epoxy matrices (70%). Here, the samples' thickness was kept as 4.0mm. First of all, the samples' dielectric parameters (the real (ε') and imaginary (ε'') parts) were measured as a function of frequency by VNA system (see Figure 4.4a). Similarly, the real (μ') and imaginary ((μ'') parts of magnetic permeability values were measured (see Figure 4.4b). The real parts of permittivity and permeability, which are responsible for electrical and magnetic storage of material system, respectively. This may impress the absorption band width in the working EMW spectrum. On the other hand, the imaginary parts of permittivity and permeability, which are responsible for electric and magnetic loss, may impress EMW absorbing rate. The magnitude of YF1000 sample's ε' value is found higher than other materials which have almost similar trend. The dielectric loss tangent ($\tan\delta_{\varepsilon}$) and magnetic loss tangent ($\tan\delta_{\mu}$) of our material systems are determined (see Figure 4.4c). Interestingly we observed that $\tan\delta_{\varepsilon}$ value is lower than $\tan\delta_{\varepsilon}$. Due to this result, it can be deduced that dielectric loss might be dominant for attenuation characteristics of EMWs in our material systems. If the materials have magnetic component, then magnetic loss can be occurred via natural resonance, exchange resonance and eddy current loss (C_0) when EMW is applied to the sample. Among them, the C_0 can be determined by following relation [31];

$$C_0 = \mu''(\mu')^{-2}f^{-1} \tag{4.2}$$

Figure 4.4d shows the eddy current loss of the samples as a function of frequency. The magnetic loss of a material system might come from eddy current loss when the C_0 remains constant in the working frequency range. Though the C_0 is nearly constant in YF700 and YF800 samples, it alters via frequency in YF900, YF1000 and YF1100 samples. This indicates that there might be other absorption mechanism in the sample structure, as well as the eddy current loss. One thing must be considered for the EMW absorption mechanism which is the attenuation. It can be defined as the ability of energy converting from microwave energy into the other types of energy when the incident EMW penetrates into the material [24, 32]. The attenuation constant (α) can be formulated as;

$$\alpha = \frac{\sqrt{2}\pi f}{c}\sqrt{(\mu''\varepsilon'' - \mu'\varepsilon') + \sqrt{(\mu''\varepsilon'' - \mu'\varepsilon')^2 + (\mu'\varepsilon'' + \mu''\varepsilon')^2}} \tag{4.3}$$

Figure 4.4d indicates the α values of our materials systems. Based on the defination of the α parameter, the higher α value means the more scattering inside of the material system. Therefore, if the α value is high, the material can absorb more EMW energy due to more scattering. In addition, though the EMW does not interact via the magnetic and/or electric components of the material, the EMW absorption can be observed via converting the penetrated EMW energy to heat/other energy due to the scattering of EMW. The highest α value was determined in YF1000 material in 8-12 GHz frequency range. In contrast, the polarization relaxation involves primarily of electron polarization, ion polarization, interface polarization, defect polarization and dipole polarization[25]. The ion and electron polarizations can be negligible in the dielectric loss because they have a tendency to be in the low frequency band [33]. Absorbing mechanism in our material system might be interfacial polarizations between $Y_3Fe_5O_{12}$ and Fe_2O_3. To analyze it, the Cole-Cole diagrams, as shown in inset of Figure 4.4d, comes from Debye theory may give further information. The semicircles in Cole-Cole plots mean the relaxation process in the working material. While our YF800, YF900 and YF1000 materials have one semicircle, YF1100 has two small semicircles that can be a proof of observing a wide bandwidth in reflection loss (see Table 4.2).

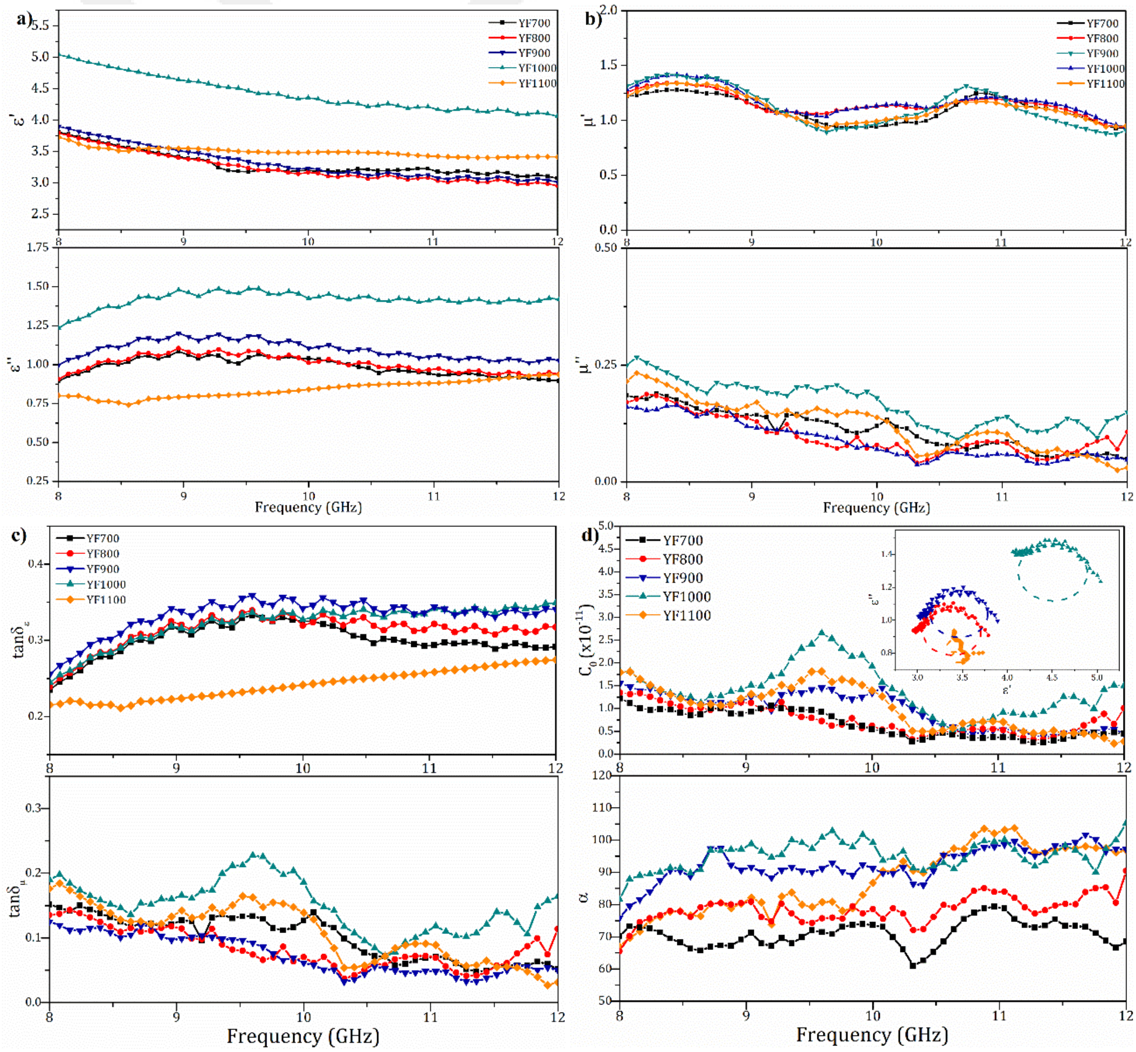

Figure 4.4. Frequency dependence of **a)** $\boldsymbol{\varepsilon}'$, $\boldsymbol{\varepsilon}''$, **b)** μ', μ'', **c)** $\tan\delta_\varepsilon$ and $\tan\delta_\mu$, **d)** C_0 and α for $Y_3Fe_5O_{12}/Fe_2O_3$ material systems.

The reflection loss (RL) of a sample is determined via the sample's dielectric parameters. The relations (4.4) and (4.5) can be used to calculate input impedance and RL [34-37];

$$Z_{in} = Z_0 \left(\sqrt{\frac{\mu_r}{\varepsilon_r}}\right) \tanh\left[j\left(\frac{2\pi f d}{c}\right)\left(\sqrt{\mu_r \varepsilon_r}\right)\right] \tag{4.4}$$

$$\mathrm{RL} = 20\log\left(\frac{Z_{in} - Z_0}{Z_{in} + Z_0}\right) \tag{4.5}$$

where Z_{in} is the input impedance of the absorber, Z_0 is impedance of air, c is the speed of EMW in the free space, f is the frequency and d is the thickness of the working material [25]. The red dashed line at -10 dB in the Figure 4.5a indicates the absorption rate of incident EMW as 90%. Although our materials can absorb incident electromagnetic wave, their absorption amount varies by ratio of $Y_3Fe_5O_{12}$ and Fe_2O_3 content. Absorbing rates of incident electromagnetic wave were found low in YF700 and YF800 materials. When the sintering temperature is increased from 800 to 900 and eventually 1000°C, materials' absorbing rate is increased due to increasing $Y_3Fe_5O_{12}$ and Fe_2O_3 interfaces. However, when the sintering temperature is increased to 1100°C, the absorbing performance of YF1100 material decreases. Since the interfaces between $Y_3Fe_5O_{12}$ and Fe_2O_3 in YF1100 sample are not as high as YF1000 sample due to melting and crystal phase amounts, the electromagnetic wave absorbing performance was decreased. Table 4.2 shows the electromagnetic wave absorbing parameters of the produced samples and some of the data in the literature for the comparison. The best electromagnetic wave absorbing perfromance having -19.5dB RL at 9.6GHz with 2.5GHz bandwith was seen in YF1000 sample. Figure 4.5b shows the $\frac{Z_{in}}{Z_0}$ as a function of frequency in the X-band of electromagnetic wave spectrum. When $\frac{Z_{in}}{Z_0}$ value is close to the 1, the impedence of the air and the material matches. In YF1000 sample, $\frac{Z_{in}}{Z_0}$ values are so close to the 1. Therefore, we can conclude that the sample sintered at 1000°C is good candidate for electromagnetic wave absorber.

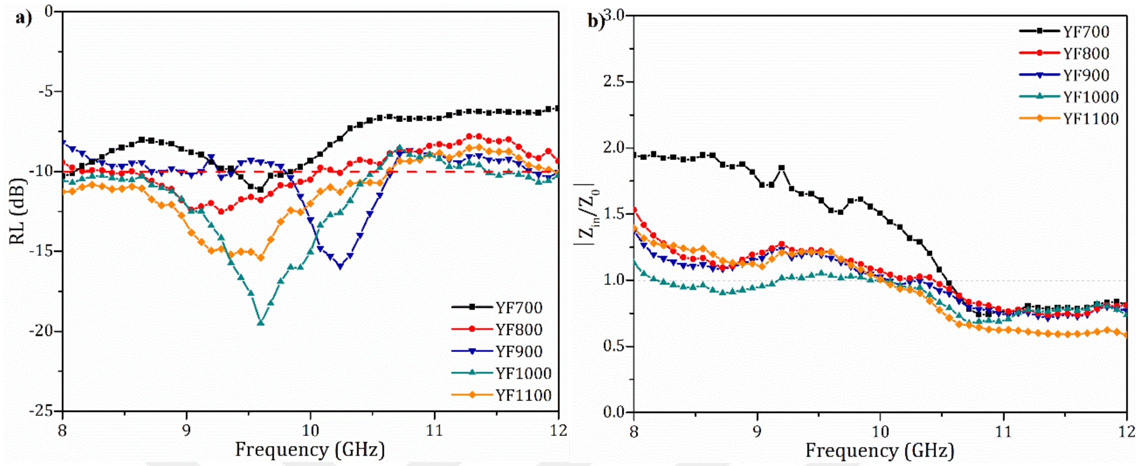

Figure 4.5. Frequency dependence of **a)** RL and **b)** $\frac{Z_{in}}{Z_0}$ values of the samples.

Table 4.2. Comparison of our materials' electromagnetic wave parameters with some works in the literature.

Sample Code	**Thickness (mm)**	**Frequency (GHz)**	**Reflection loss (dB)**	**Band width (GHz)**	**References**
YIG	2.0	9.8	-7.2	4.2	[38]
γ-Fe_2O_3	3.0	9.2	-12.3	1.6	[39]
YF700		9.5	-11.2	0.5	
YF800		9.3	-12.5	1.5	
YF900	4.0	10.3	-15.9	0.9	Our samples
YF1000		9.5	**-19.5**	2.5	
YF1100		9.6	-15.4	**2.6**	

4.2. Study on the Effect of Carbon Black on Structure, Magnetic and Electromagnetic Properties in YIG_{1-x}/CB_x Composites

Carbon black (CB) material is an electrical loss material having low density, which is commonly used as the carrier of strong microwave absorbing materials and the matching layer of multilayer absorbers [40]. CB itself has narrow absorption band and weak absorption performance. When it is used as microwave absorption material alone, the impedance-matching characteristics of the absorption layer becomes poor, because of its large dielectric constant. [41]. Therefore, when the YIG and carbon black are used together, the composite absorbent has both magnetic loss and electrical loss, which reduces the density of the microwave-absorbing material and effectively broadens the absorption frequency band. Here, we study the effect of carbon black on the structure, magnetic and electromagnetic properties of YIG_{1-x}/CB_x (x=0.00, 0.25, 0.50, 0.75 and 1.00) composites.

4.2.1. Structural properties of YIG_{1-x}/CB_x composites

Structural properties of the synthesized YIG_{1-x}/CB_x (x=0.00, 0.25, 0.50, 0.75 and 1.00) composite powders are studied by measuring XRD in between $10^o \leq 2\theta \leq 90^o$. Figure 4.6 shows the XRD patterns of YIG, $YIG_{0.75}/CB_{0.25}$, $YIG_{0.50}/CB_{0.50}$, $YIG_{0.25}/CB_{0.75}$, CB samples called as YCB1, YCB2, YCB3, YCB4 and YCB5, respectively. The XRD data were analyzed by X-Pert High Score software. The YIG crystalline properties have been already optimized in Section 4.1. Thus, we just checked the characteristic YIG peaks in the XRD spectrum that they are all consistent with the data in Section 4.1.1. On the other hand, the carbon black crystal structure showed the crystaline peaks at 25.1° and 43.0° with diffraction planes of (002) and (101), respectively. As expected, the intensity of CB (YIG) crystalline peaks increase (decrease) with the content of CB in the composites.

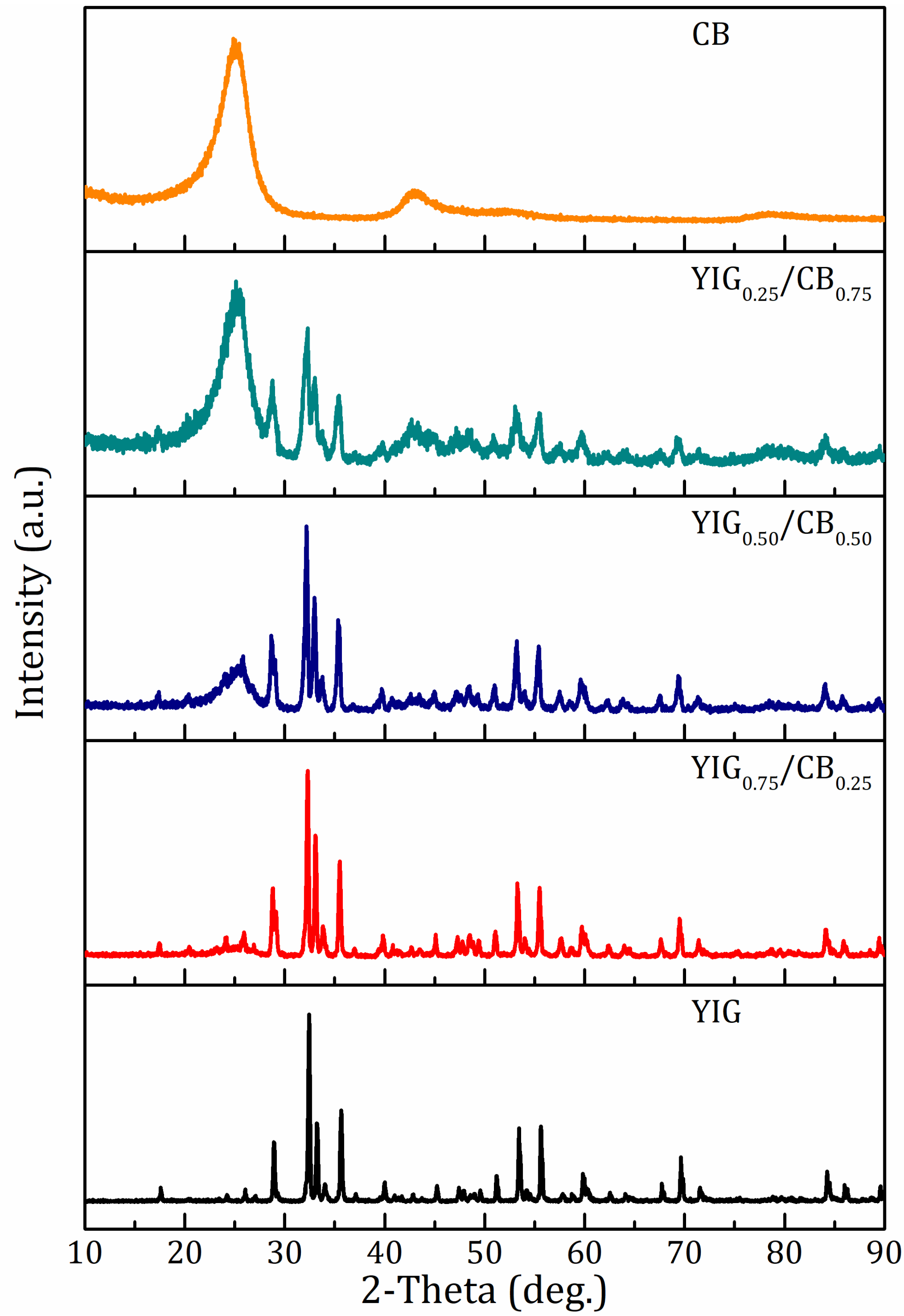

Figure 4.6. XRD patterns of YIG_{1-x}/CB_x (x:0.00, 0.25, 0.50, 0.75 and 1.00) composites.

4.2.2. Morphological properties of YIG_{1-x}/CB_x composites

The surface morphologies of the produced YIG_{1-x}/CB_x ($0.00 \leq x \leq 1.00$; 0.25 steps) composites were studied by taking SEM images at various magnifications (5KX, 50KX and 100KX). Figures 4.7, 4.8, 4.9, 4.10 and 4.11 show the SEM images of YIG, $YIG_{0.75}/CB_{0.25}$, $YIG_{0.50}/CB_{0.50}$, $YIG_{0.25}/CB_{0.75}$ and CB samples, repectively. At low magnification (5KX), it is seen that the grains are distributed homogenously through the samples. Once the magnification is increased to 50KX and 100KX, the grain boundaries are seen easily, especially in YIG sample. Due to the spherical morphology and small grain size of CB (see Fig.4.11c), the overall grain size is reduced by increasing the concentration of CB in the composites.

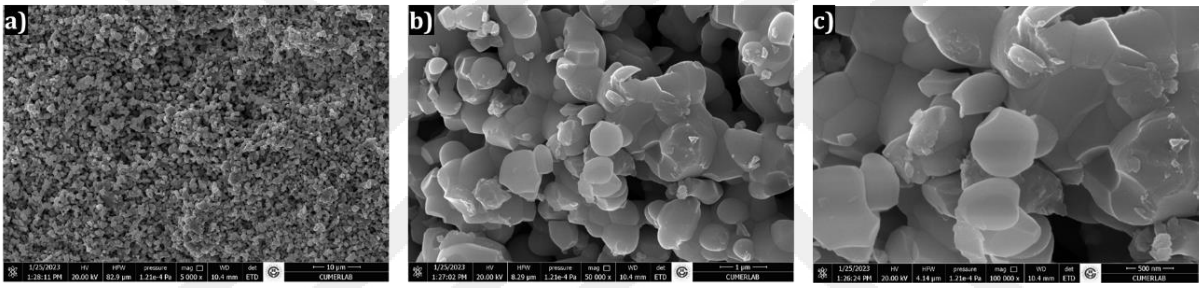

Figure 4.7. SEM images of YIG samples taken at **a)** 5KX, **b)** 50KX and **c)**100KX magnifications.

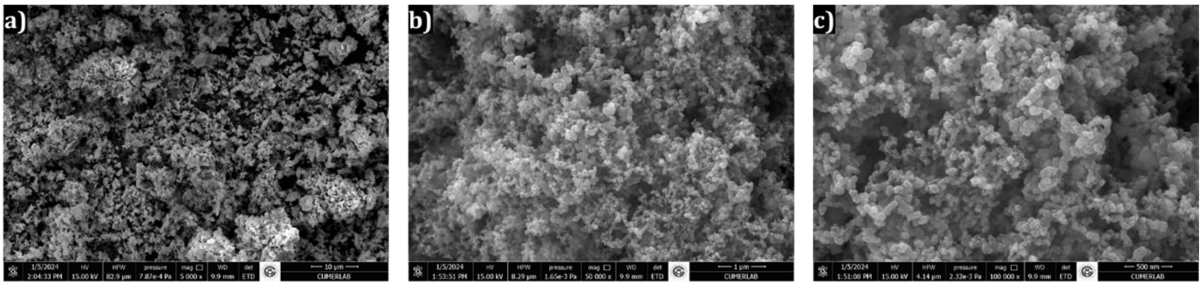

Figure 4.8. SEM images of $YIG_{0.75}/CB_{0.25}$ composites taken at **a)** 5KX, **b)** 50KX and **c)**100KX magnifications.

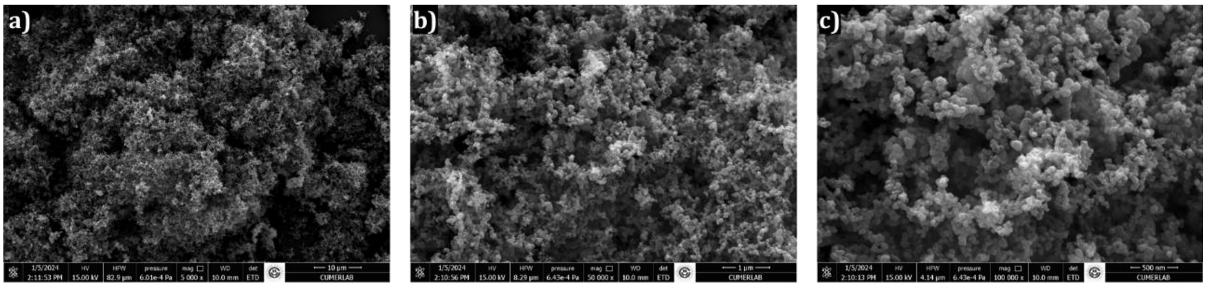

Figure 4.9. SEM images of $YIG_{0.50}/CB_{0.50}$ composites taken at **a)** 5KX, **b)** 50KX and **c)**100KX magnifications.

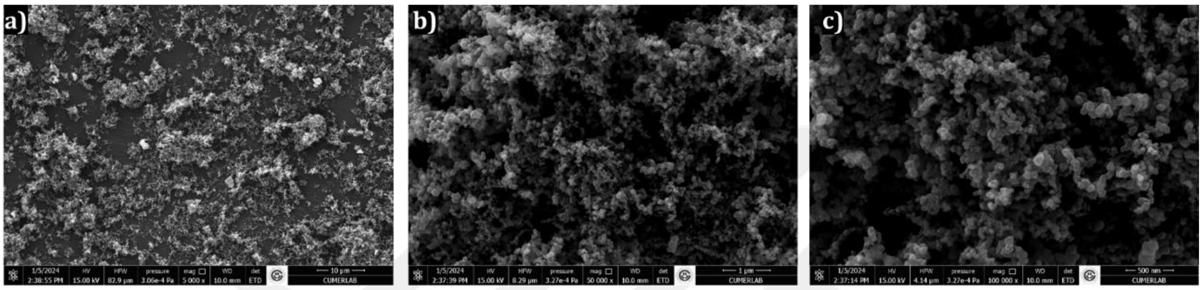

Figure 4.10. SEM images of $YIG_{0.25}/CB_{0.75}$ composites taken at **a)** 5KX, **b)** 50KX and **c)**100KX magnifications.

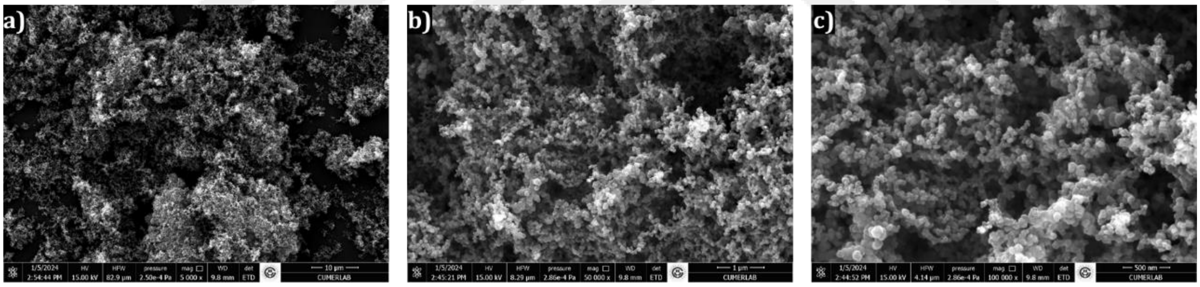

Figure 4.11. SEM images of CB samples taken at **a)** 5KX, **b)** 50KX and **c)**100KX magnifications.

4.2.3. Magnetic properties of YIG_{1-x}/CB_x composites

The magnetic hysteresis (*M-H*) loops of the YIG_{1-x}/CB_x (x=0.00, 0.25, 0.50, 0.75 and 1.00) composites are shown in Figure 4.12a. The *M-H* loops were measured at 300K under ±30 kOe magnetic field. Except CB sample, the composites have similar *M-H* loops having almost zero coercieve field and remenant magnetization. As expected the M_s increases with the

$Y_3Fe_5O_{12}$ content in YIG_{1-x}/CB_x composites (see Figure 4.12b). Since CB is not a magnetic material, the magnetic response under applied magnetic field is almost zero.

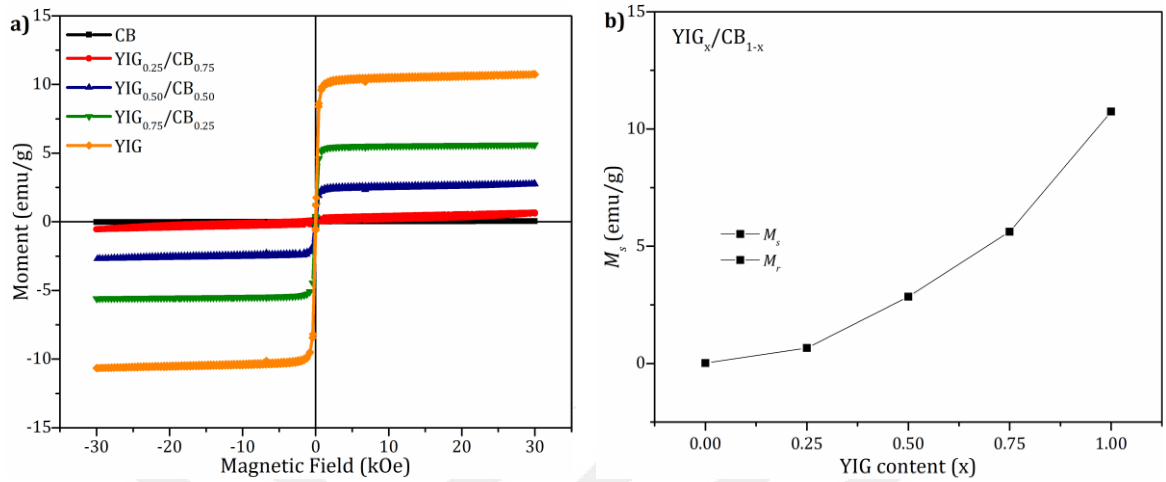

Figure 4.12.a) *M-H* curves of YIG_{1-x}/CB_x composites, **b)** M_s versus YIG content in the composites.

4.2.4. Electromagnetic properties of YIG_{1-x}/CB_x composites

Electromagnetic wave absorbing properties of YIG_{1-x}/CB_x (x=0.00, 0.25, 0.50, 0.75 and 1.00) composites were worked in between 2-18 GHz frequency range of the electromagnetic wave spectrum. The impact of the YIG and CB contents on the EMW properties in YIG_{1-x}/CB_x composites was studied by fixing their thickness in the epoxy matrices as 4.0mm. The curing process is same as we used in other samples (see Section 3.5.3 and Section 4.1.4). As explained in the Section 4.1.4, the same measurement method was used to work on the electromagnetic wave absorption performance of the YIG_{1-x}/CB_x (x=0.00, 0.25, 0.50, 0.75 and 1.00) composites. Figure 4.13a-b show the real (ε') and imaginary (ε'') parts of permittivity of the YIG_{1-x}/CB_x (x=0.00, 0.25, 0.50, 0.75 and 1.00) composites as a function of frequency, respectively. The trend in ε' values of all samples is similarly decreases with increasing frequency. The maximum ε' was observed in $YIG_{0.25}/CB_{0.75}$ composite. The relative magnetic permeability values (μ' and μ'') as a function of frequency is shown in Figure 4.13c-d, respectively. While the YIG has a wavy signal in both μ' and μ'', smooth decreasing trend appears in other samples.

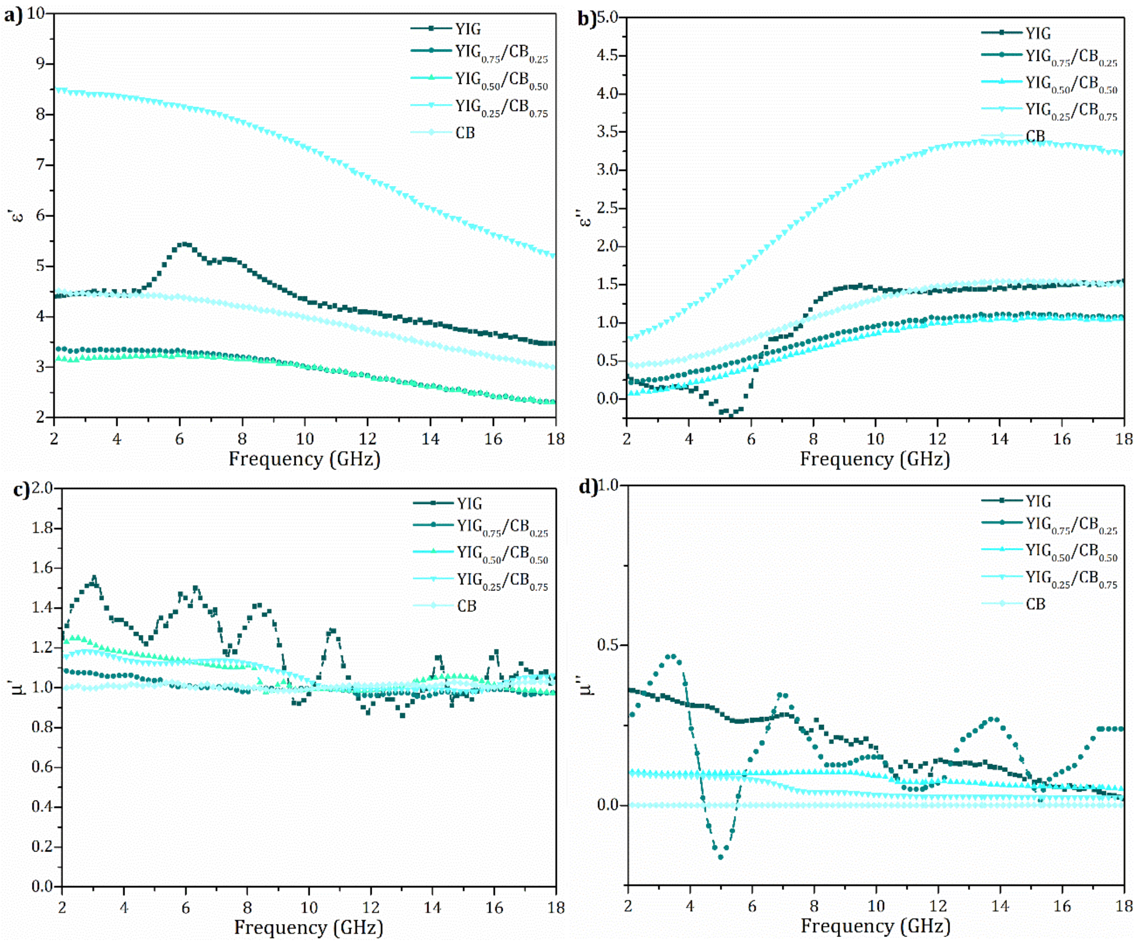

Figure 4.13. Frequency dependence of **a)** ε', **b)** ε'', **c)** μ' and **d)** μ'' for YIG_{1-x}/CB_x composites.

The loss tangent parameters ($\tan\delta_\varepsilon$ and $\tan\delta_\mu$) for YIG_{1-x}/CB_x (x=0.00, 0.25, 0.50, 0.75 and 1.00) composites are calculated and plotted in Figure 4.14a-b, respectively. The $\tan\delta_\varepsilon$ values of the samples increase with the frequency between 2 and 18 GHz. On the other hand, the magnitude of $\tan\delta_\mu$ values reduces with the increasing CB content in the YIG_{1-x}/CB_x composites.

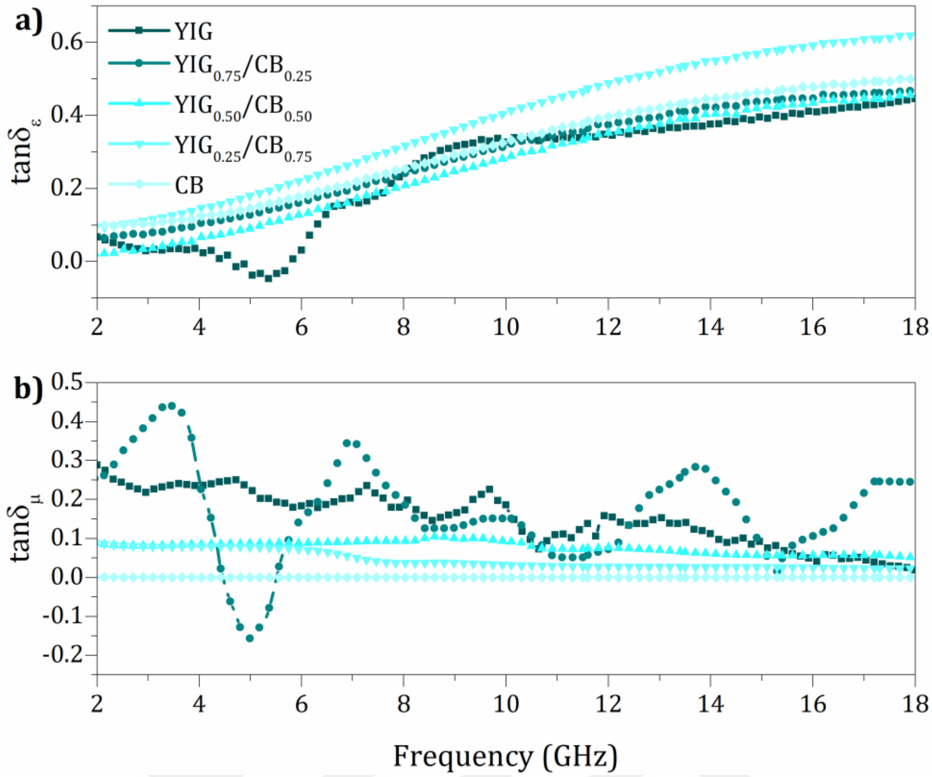

Figure 4.14.a) $\tan\delta_\varepsilon$ and **b)** $\tan\delta_\mu$ as a function of frequency curves for YIG_{1-x}/CB_x composites.

As we calculated in Section 4.1.4, the α values of YIG_{1-x}/CB_x composites were calculated by using Eq.(4.5). Figure 4.15a shows the attenuation constant of YIG_{1-x}/CB_x composites. The highest α value is seen in $YIG_{0.25}/CB_{0.75}$ composite. It means the EMW can be scattered more in the $YIG_{0.25}/CB_{0.75}$ composite than the other composites. Therefore, the absorption performance of this composite might be better than others. The dielectric loss of our samples is mainly caused by carbon black itself and interfacial polarizations between YIG and CB. The eddy current loss of composites calculated by using Eq.(4.4) are shown in Figure 4.15b. If the magnetic loss of the materials is only due to eddy current, the value of C_0 should remain constant in the frequency variation. The magnitude of C_0 values of CB is almost zero in between 2-18 GHz frequency range. Once the YIG content is increased in the composite, it starts to increase at low frequency range.

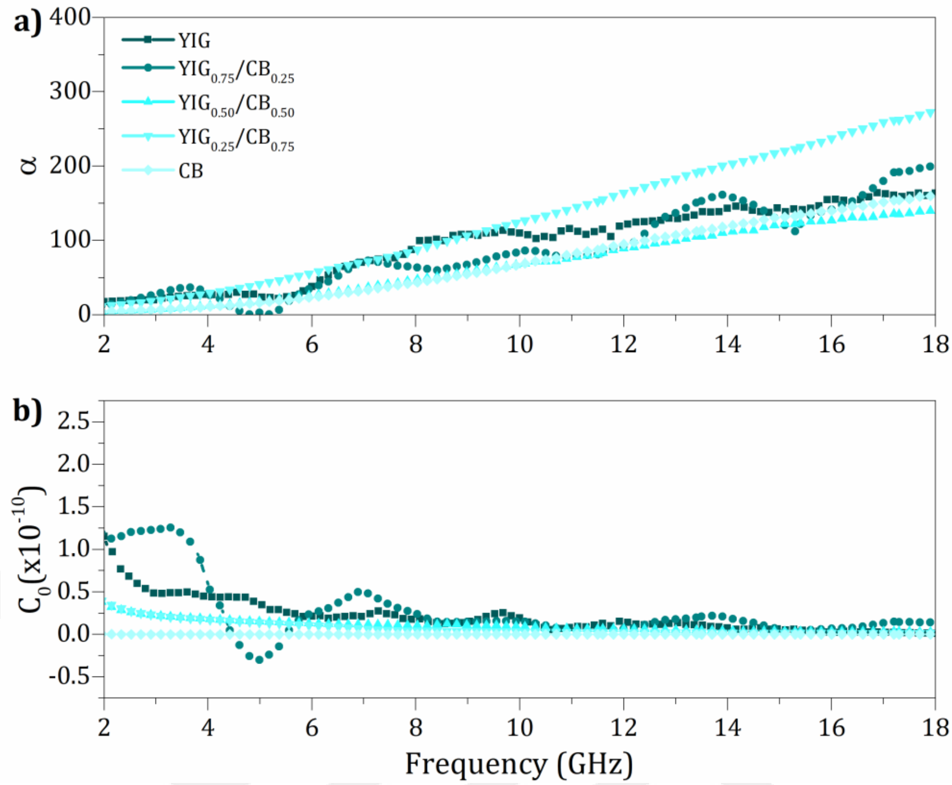

Figure 4.15.a) Attenuation constant and **b)** Eddy-current loss as function of frequency curves for YIG_{1-x}/CB_x composites.

As explained in Section 4.1.4, the RL values of YIG_{1-x}/CB_x composites were calculated based on the relative complex permittivity (ε_r) and relative complex permeability (μ_r) values using Eq.(4.4) and (4.5). Figure 4.16a shows the RL curves of YIG_{1-x}/CB_x composites as a function of frequency. The line shown as a red dashed at -10 dB in the Figure 4.16a indicates the 90% absorption rate. This value in RL curve means that the 90% of incident electromagnetic wave is absorbed. Since the RL curves gives the absorption rate of the materials in the working frequency, the maximum absorption rate and bandwidth can be extracted from RL-frequency curves. Although all samples absorb some of the incoming EMWs, the absorption rate changes by the ratio of YIG and CB content in the composite. The broadband electromagnetic wave absorbing (8.1 GHz) at -10 dB was observed in $YIG_{0.75}/CB_{0.25}$ composite. This indicates that the 90% of the incoming electromagnetic wave can be absorbed in between 9.9 GHz and 18 GHz. The minimum reflection loss was observed as -19.09 dB at 13.54 GHz frequency. Since the absorption mechanism directly related with impedance matching between incident and penetrated mediums and the electrical and magnetic losses of the material in which EMW propagates, the impedance matching is provided between 2-18 GHz frequency range in Figure 4.16b.

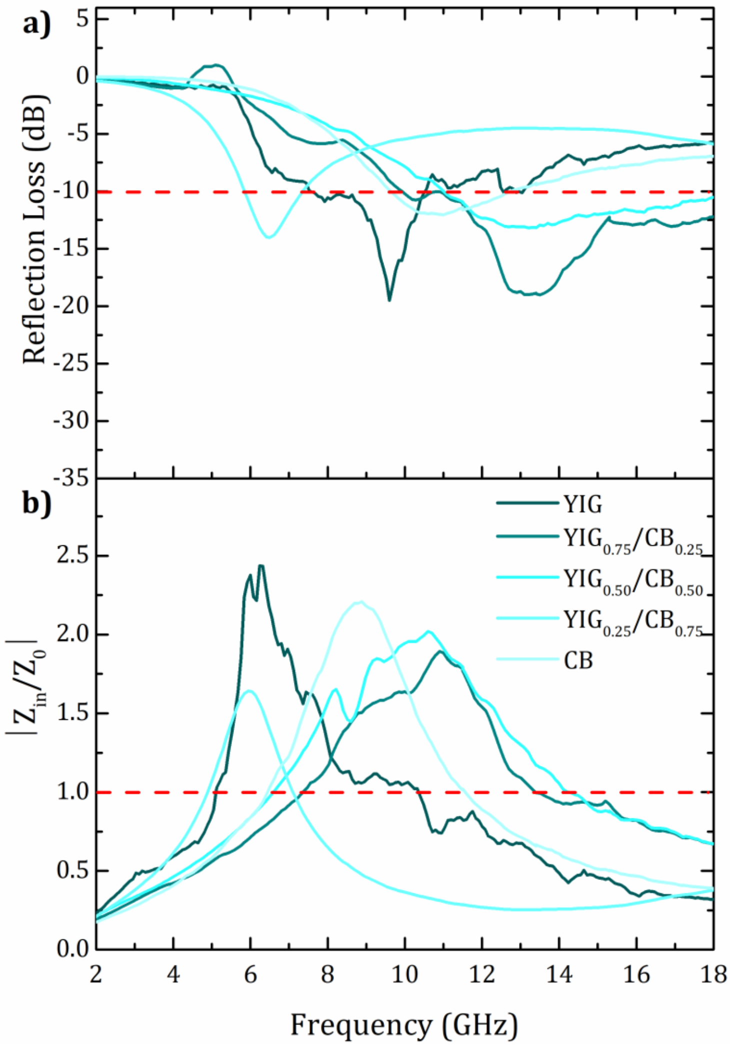

Figure 4.16. Frequency dependence of **a)** RL and **b)** $\frac{Z_{in}}{Z_0}$ values of YIG_{1-x}/CB_x composites.

Table 4.3. Comparison of our YIG_{1-x}/CB_x (x=0.00, 0.25, 0.50, 0.75 and 1.00) composites' electromagnetic wave parameters with some works in the literature.

Sample Code	Thickness (mm)	Frequency (GHz)	Reflection loss (dB)	Band width (GHz)	References
YIG	2.0	9.8	-7.2	4.2	[38]
YIG	4.0	9.5	-19.5	2.5	Our samples
$YIG_{0.75}/CB_{0.25}$		13.5	-19.1	8.1	
$YIG_{0.50}/CB_{0.50}$		13.2	-13.1	7.1	
$YIG_{0.25}/CB_{0.75}$		6.5	-14.2	1.5	
CB		10.8	-12.0	3.1	

4.3. Conductive Polyaniline Coated PANI@YIG_{1-x}/CB_x Hybrid Composites

In this section, the YIG_{1-x}/CB_x composites composites were coated with the conductive polianiline (PANI) polymer to enhance the electromagnetic loss properties of the samples. Conductive polianiline polymer is an electrical loss material having low density similar to the carbon black. Since CB, YIG and PANI itself have narrow absorption band and weak absorption performance, it is commonly used as a composite forms to enhance the electromagnetic wave absorbing performance by tuning the impedance-matching. Therefore, when the YIG, CB and PANI are used together, the hybrid composite absorbent might behave high performance radar absorbing properties. Thus, here, we study the effect of conductive PANI polymer on the structure, magnetic and electromagnetic properties of PANI@YIG_{1-x}/CB_x composites.

4.3.1. Structural properties of PANI@YIG_{1-x}/CB_x hybrid composites

Structural properties of the conductive polyaniline coated PANI@YIG_{1-x}/CB_x (x=0.00, 0.25, 0.50, 0.75 and 1.00) composite powders were examined by XRD between $5º\leq 2\theta \leq 90º$. Figure 4.17 shows the XRD patterns of PANI@YIG, PANI@$YIG_{0.75}/CB_{0.25}$, PANI@$YIG_{0.50}/CB_{0.50}$, PANI@$YIG_{0.25}/CB_{0.75}$, PANI@CB samples called as PYCB1, PYCB2, PYCB3, PYCB4 and PYCB5, respectively. Since the YIG materials' crystal structure has been investigated in Section 4.1.1, we are not deeply analyze the XRD peaks of the YIG. The characteristic YIG cyrstalline peaks have been observed in the XRD spectrum (see Fig.4.17) which are consistent with the data observed in Section 4.1.1. On the other hand, the carbon black crystal structure showed the crystaline peaks at 25.1° and 43.0° with diffraction planes of (002) and (101), respectively. As expected, the intensity of CB (YIG) crystalline peaks increase (decrease) with the content of CB in the composites. Although the PANI content was kept constant in all hybrid composites, the PANI crystalline peaks appears more clear in PANI@CB sample since CB's crystalline intenstiy is lower than the YIG sample.

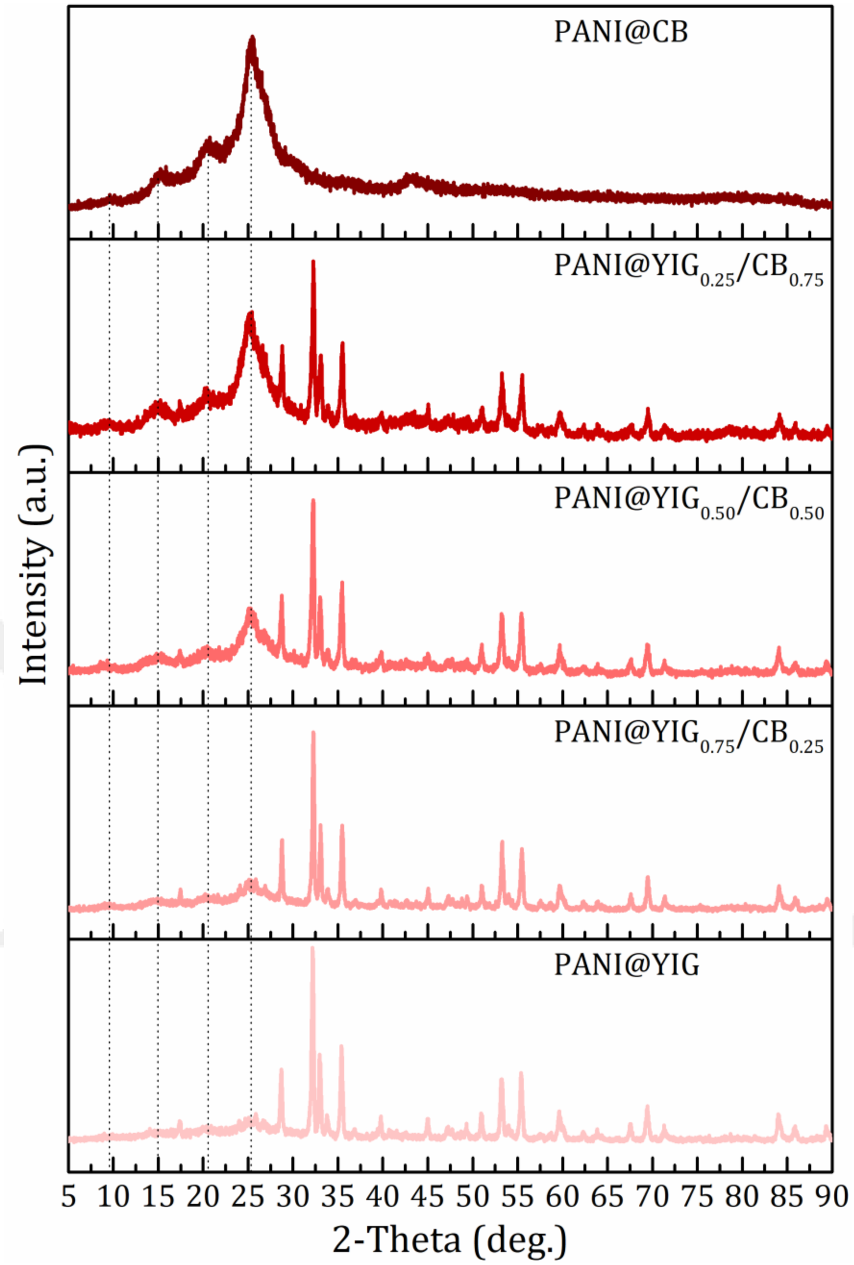

Figure 4.17. XRD patterns of PANI coated YIG_{1-x}/CB_x (x:0.00, 0.25, 0.50, 0.75 and 1.00) hybrid composites.

4.3.2. Magnetic properties of PANI@YIG_{1-x}/CB_x hybrid composites

The magnetic hysteresis (*M-H*) loops of the PANI@YIG_{1-x}/CB_x (x=0.00, 0.25, 0.50, 0.75 and 1.00) composites measured at 300K are shown in Figure 4.18. Since PANI polymer does not exhibit magnetic characteristic, the magnetic signals of its composites become also weak.

Especially, the PANI@CB sample shows almost diamagnetic characteristic because two of its components have no magnetic characteristic. Once the YIG content increased in the hybrid composites, the magnetization starts to enhance and finally it almost behaves like a single YIG magnetic characteristic in PANI@YIG hybrid composite. In addition, only PANI@YIG and PANI@$YIG_{0.75}$/$CB_{0.25}$ hybrid nanocomposites have saturation magnetization. All hybrid composites have almost zero coercieve field and remenant magnetization.

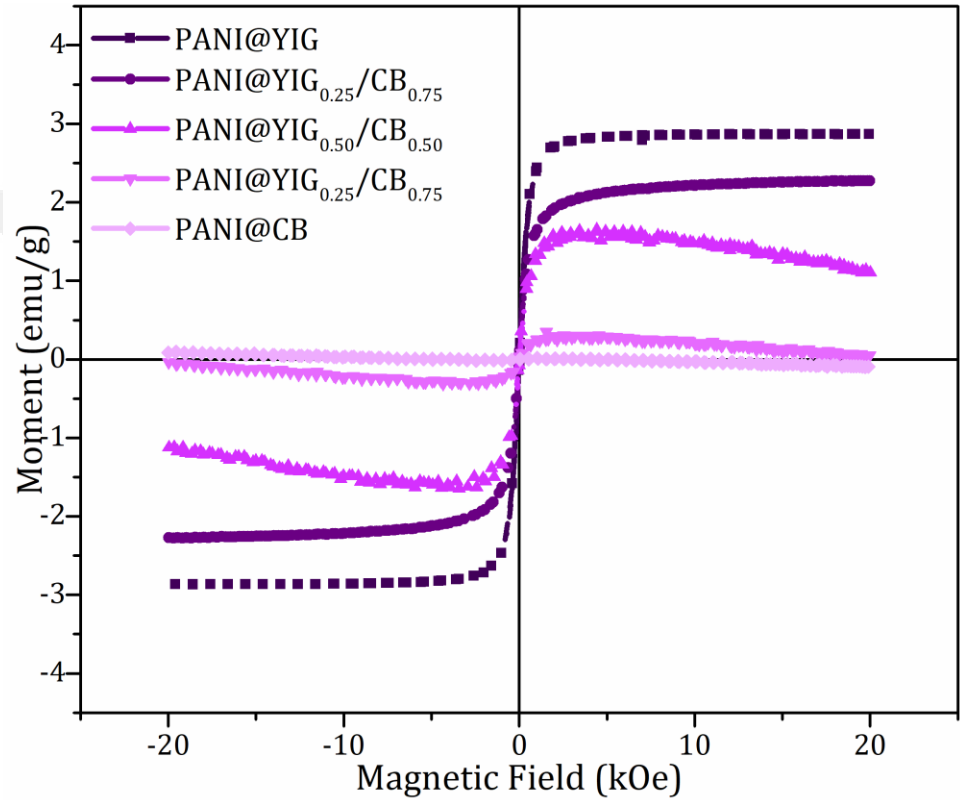

Figure 4.18. *M-H* curves of PANI coated YIG_{1-x}/CB_x ($0.00 \leq x \leq 1.00$) hybrid composites.

4.3.3. Electromagnetic properties of PANI@YIG_{1-x}/CB_x hybrid composites

The EMW absorbing performance of the PANI@YIG_{1-x}/CB_x (x=0.00, 0.25, 0.50, 0.75 and 1.00) hybrid composites were studied in the 2-18 GHz frequency range of electromagnetic wave spectrum. In order to investigate the impact of the YIG and CB contents on the EMW properties in PANI@YIG_{1-x}/CB_x composites, the PANI content and thickness of the composites embedded in the epoxy matrices were fixed as 50% and 4 mm, respectively.

Figure 4.19a-b show the real (ε') and imaginary (ε'') parts of permittivity of the PANI@YIG_{1-x}/CB_x (x=0.00, 0.25, 0.50, 0.75 and 1.00) hybrid composites as a function of frequency, respectively. The maximum ε' was observed in PANI@YIG and PANI@$YIG_{0.75}$/$CB_{0.25}$ hybrid composites. The relative magnetic permeability values (μ' and μ'') as a function of frequency are shown in Figure 4.19c-d, respectively.

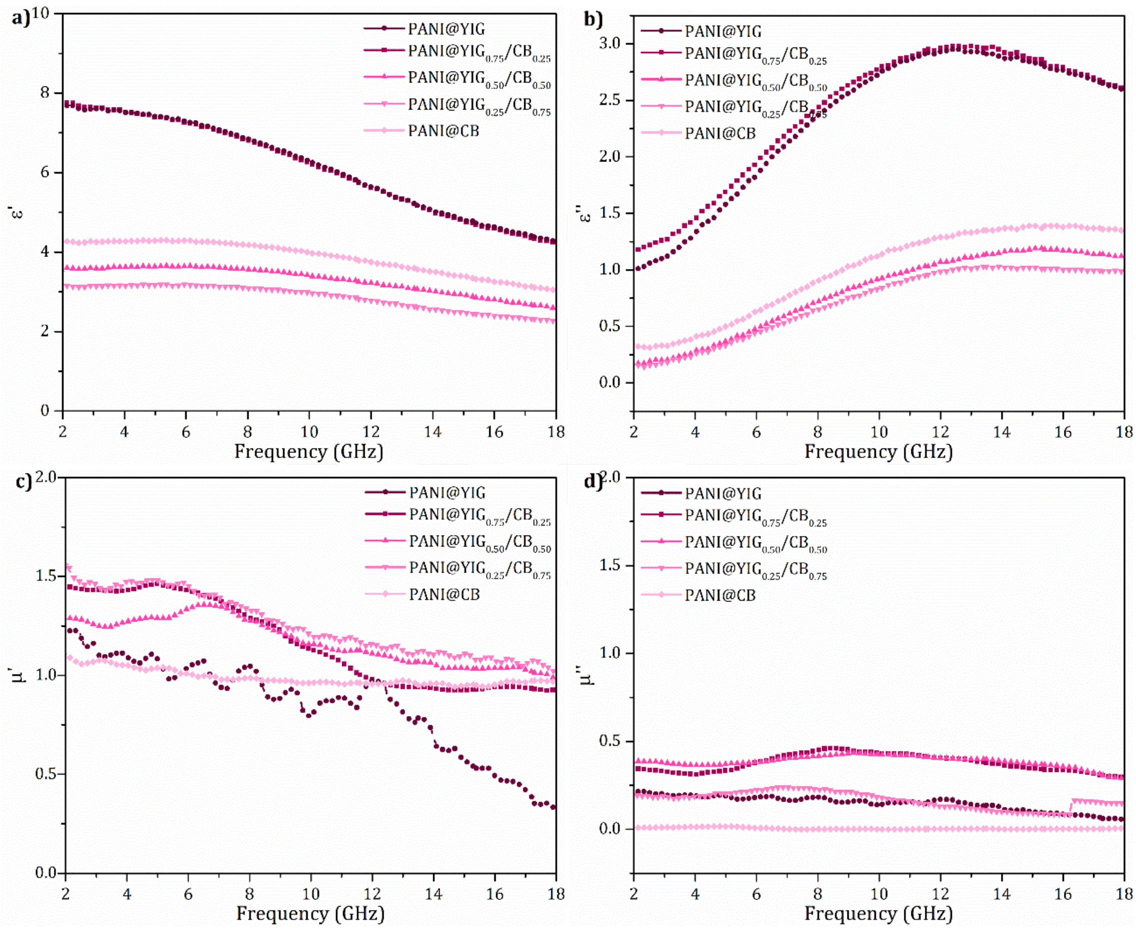

Figure 4.19.a) Relative real, **b)** imaginary parts of permittivity, **c)** relative real and **d)** imaginary parts of permeability of PANI coated YIG_{1-x}/CB_x (x:0.00, 0.25, 0.50, 0.75 and 1.00) hybrid composites.

The loss tangent values ($\tan\delta_\varepsilon$ and $\tan\delta_\mu$) of YIG_{1-x}/CB_x (x=0.00, 0.25, 0.50, 0.75 and 1.00) composites are calculated and plotted in Figure 4.20a-b, respectively. The $\tan\delta_\varepsilon$ values of the samples increase with the frequency between 2 and 18 GHz. On the other hand, the magnitude of tanδ_μ values reduces with the increasing CB content in the YIG_{1-x}/CB_x composites.

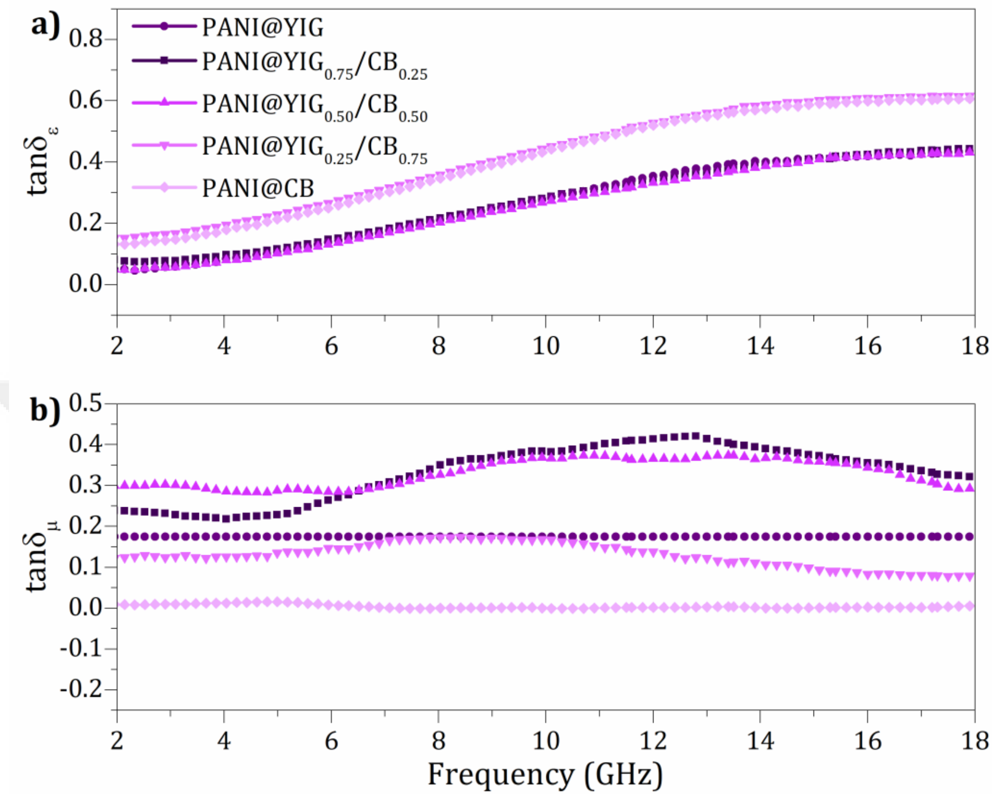

Figure 4.20.a) tanδ_ε and **b)** tanδ_μ as a function of frequency curves of PANI coated YIG_{1-x}/CB_x (x:0.00, 0.25, 0.50, 0.75 and 1.00) hybrid composites.

The α values of the PANI@YIG_{1-x}/CB_x (x:0.00, 0.25, 0.50, 0.75 and 1.00) hybrid composites were calculated by using Eq.(4.5). Figure 4.21a shows the attenuation constant of PANI@YIG_{1-x}/CB_x (x:0.00, 0.25, 0.50, 0.75 and 1.00) hybrid composites. A similar behaviour is observed in all samples that the α values increase with the increase of frequency, except PANI@YIG sample whose attenuation value saturate after 12 GHz frequency. The highest α value is observed in PANI@$YIG_{0.25}/CB_{0.75}$ hybrid composite. If the materials have magnetic characteristic, they may show magnetic loss that is related to natural resonance, exchange resonance and eddy current loss (C_0), which can provide information for the attenuation capacity of the samples. Since our composites have magnetic component, we calculated the eddy current loss. The C_0 can be calculated by using Eq.(4.4). Figure 4.21b shows the C_0 values of the hybrid composites as a function of frequency. The C_0 values of PANI@CB composite is almost zero in between 2 and 18 GHz frequency range that this composite does not have magnetic component. Once the YIG introduces into the hybrid composites, magnetic loss of them increases. Almost in all samples, the C_0 values become constant above 6 GHz that indicates the magnetic loss mechanism by eddy current loss.

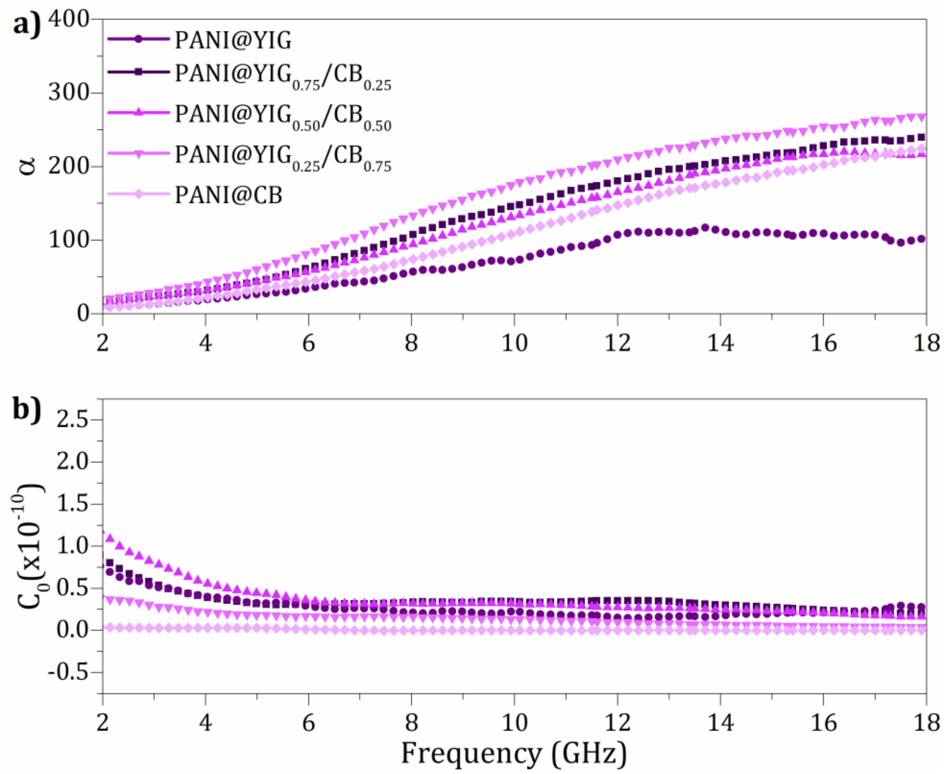

Figure 4.21.a) Attenuation constant and **b)** Eddy-current loss as function of frequency curves of PANI coated YIG_{1-x}/CB_x (x:0.00, 0.25, 0.50, 0.75 and 1.00) hybrid composites.

The RL values of PANI@YIG_{1-x}/CB_x hybrid composites were calculated by using Eq.(4.4) and (4.5). Figure 4.22a shows the RL curves of PANI@YIG_{1-x}/CB_x composites as a function of frequency between 2 and 18 GHz. As explained in Section 4.1.4 and 4.2.3, the RL values indicates the absorption rate of the material system. Although all samples absorb some of the incoming EMWs, the absorption rate alters with the amount of YIG and CB content in the PANI@YIG_{1-x}/CB_x hybrid composite. The broadband electromagnetic wave absorbing (10.2

GHz) at -10 dB was observed in PANI@$YIG_{0.50}$/$CB_{0.50}$ hybrid composite. This indicates that the 90% of the incident EMW can be absorbed in between 7.8 GHz and 18 GHz. The minimum reflection loss was observed as -20.0 dB at 10.5 GHz frequency. Since the absorption mechanism directly is related with impedance matching between incident and the penetrated mediums and the electrical and magnetic losses of the material in which EMW propagates, the impedance matching is provided between 2-18 GHz frequency range in Figure 4.22b.

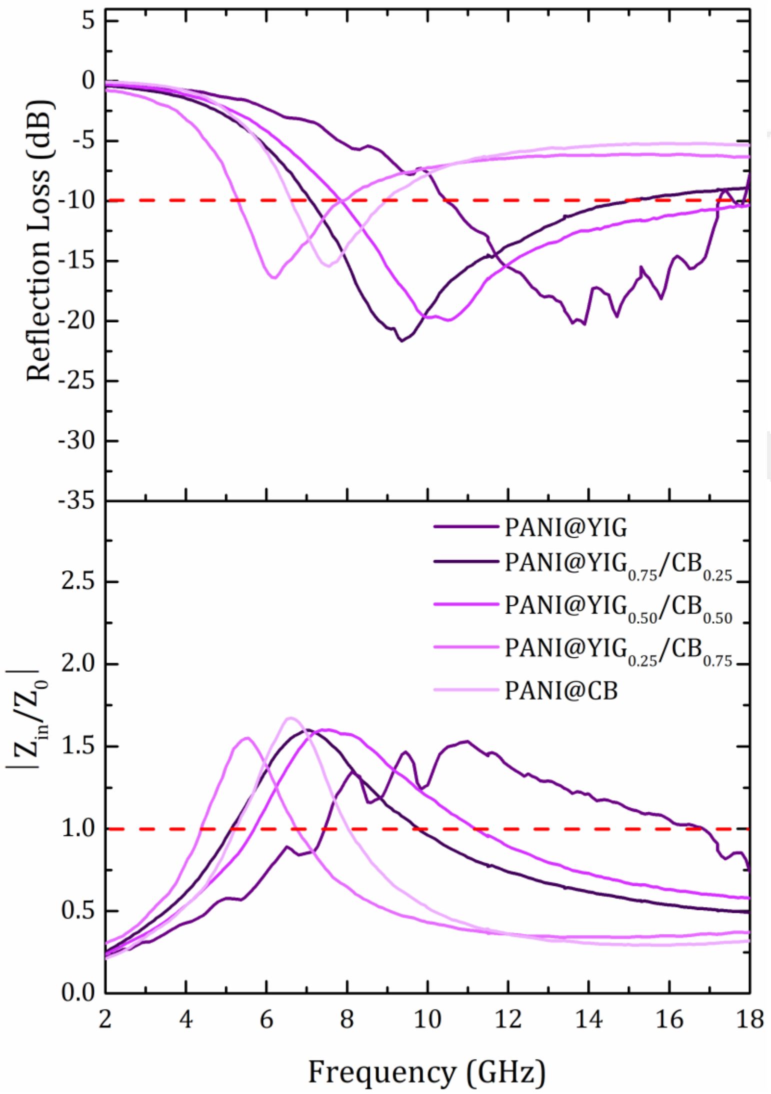

Figure 4.22. Frequency dependence of **a)** RL and **b)** $\frac{Z_{in}}{Z_0}$ values of PANI@YIG_{1-x}/CB_x (x:0.00, 0.25, 0.50, 0.75 and 1.00) hybrid composites.

Table 4.4. Comparison of our PANI@ YIG_{1-x}/CB_x (x=0.00, 0.25, 0.50, 0.75 and 1.00) hybrid composites' electromagnetic wave parameters with some works in the literature.

Sample Code	**Thickness (mm)**	**Frequency (GHz)**	**Reflection loss (dB)**	**Band width (GHz)**	**References**
YIG	2.0	9.8	-7.2	4.2	[38]
$YIG_{0.75}/CB_{0.25}$	4.0	9.5	-19.5	2.5	Our samples
$YIG_{0.50}/CB_{0.50}$		13.5	-19.1	8.1	
$YIG_{0.25}/CB_{0.75}$		13.2	-13.1	7.1	
CB		6.5	-14.2	1.5	
PANI@YIG		9.4	-21.7	8.3	
PANI@$YIG_{0.75}/CB_{0.25}$		13.9	-20.2	6.8	
PANI@$YIG_{0.50}/CB_{0.50}$		10.5	-20.0	10.2	
PANI@$YIG_{0.25}/CB_{0.75}$		6.2	-16.5	2.6	
PANI@CB		7.6	-15.4	2.4	

4.4. Application of Advanced Radar Absorbing Hybrid Composites as Camouflage Paint in the Military Land Vehicles

The hybrid composites discussed in Section 4.3 were used as a packing materials for camouflage paint on Miilux Protection 600 HB series steel. This series steel is used as an armor steel which protects the military land vehicles from the possible attacks. In addition to its armor property, we added radar stealth technology. To do this, first of all, sandblasting was applied to the steel. After that, the water-based paint were mixed with the hybrid composite in an appropriate amount. Then, the curing (60°C) process was applied. The obtained additive paint was applied to the sandblasted Miilux P600T armor steel surface having 30cm×30cm dimensions by spray application method (see Figure 4.23).

Ballistic tests were carried out in accordance with STANAG 4569 AEP 55 Vol 1 Level 2 in order to confirm that the resulting mixture does not create ballistic vulnerabilities during the application process to armor steel. 10 shots were made with 7.62x 39 API BZ ammunition. It was determined that all PP (Partial Penetration) full protection was provided. According to the terminal ballistics, there are no domes or cracks on the surface as shown in Figure 4.23. Due to the armor-piercing and flame-throwing properties of the ammunition, white shadows appeared on the surface due to high temperatures. The formation of fluctuations is a stable situation as it has no effect on penetration. When evaluated in general terms, the advanced hybrid radar absorbing composite materials as a packing in the water-based paint mixture can be used in the armor steel to add new function to the military land vehicles.

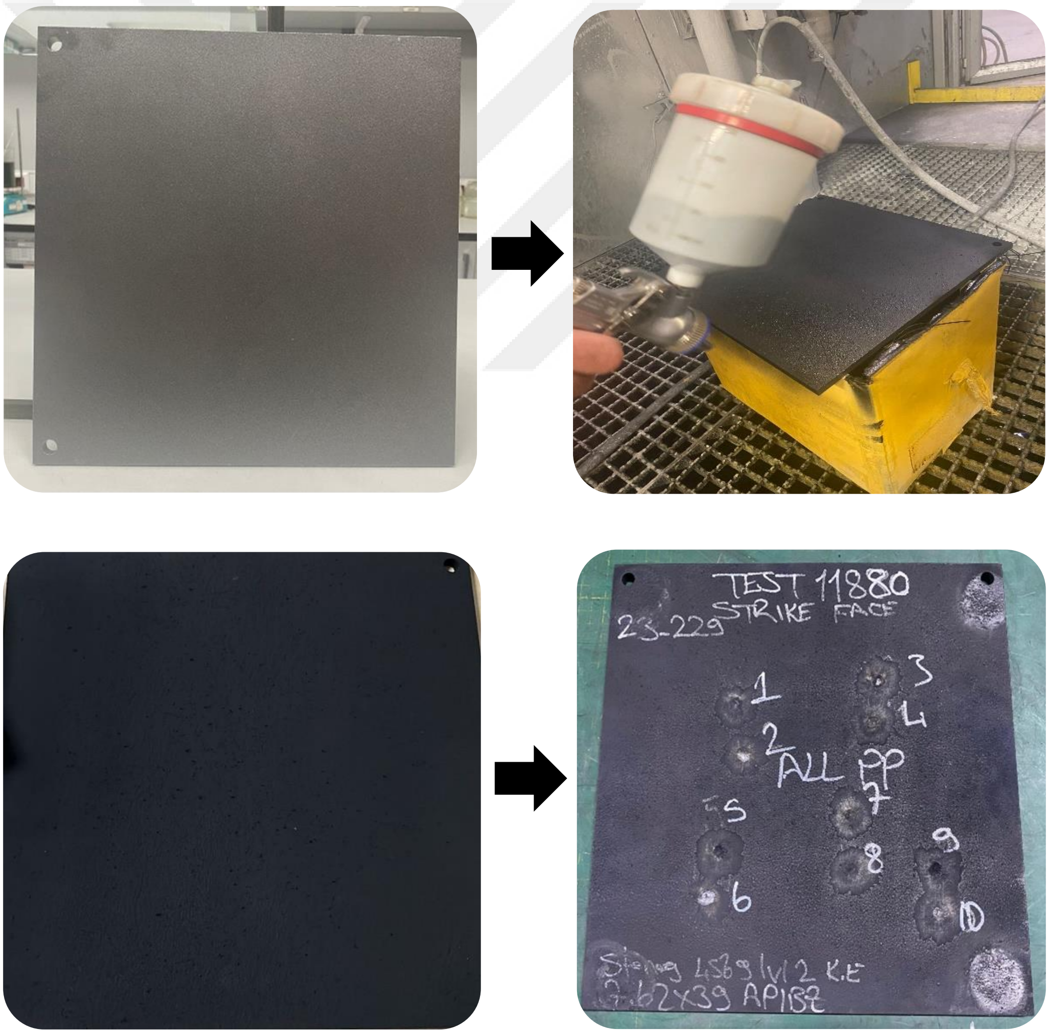

Figure 4.23. The armor steel’s painting and ballistic test results.

5. CONCLUSIONS

In summary, the sintering temperature effect on the structure, morphology, magnetic and electromagnetic absorbing properties of $Y_3Fe_5O_{12}$ has been studied in detail in this work. As the sintering temperature increases, the YIG crystals become dominant by increasing average grain and crystallite sizes. Due to the weak Fe_2O_3 crystal phase in the whole structure, it induced an interface polarization and then enhanced the electromagnetic absorption properties of the samples. The minimum reflection loss has been determined as -19.54 dB at 9.59 GHz frequency with 2.52 GHz bandwidth in YF1000 sample.

The YIG_{1-x}/CB_x (x=0.00, 0.25, 0.50, 0.75 and 1.00) composites synthesized by solid-state reaction method indicate both YIG and CB crystalline peaks in the composites. The magnetic saturation value of the composites reduced with the increasing CB content in the composites. The EMW performance of the composites showed a broadband absorption properties (8.1 GHz bandwidth at -10dB reflection loss value) in $YIG_{0.75}/CB_{0.25}$ composite. This indicates that the 90% of the incoming electromagnetic wave can be absorved in between 9.9 GHz and 18 GHz. The minimum reflection loss was observed as -19.09 dB at 13.54 GHz frequency.

The YIG_{1-x}/CB_x composites were coated with the conductive polianiline (PANI) polymer to enhance the electromagnetic loss properties of the samples. Conductive polianiline polymer is an electrical loss material having low density similar to the carbon black. The experimental results indicate that the covering of YIG/CB composites with PANI polymer boost the EMW performance of the materials. The highest EMW absorbing performance was observed in PANI@$YIG_{0.50}/CB_{0.50}$ hybrid composite having 10.2 GHz effective bandwidth at -10 dB. This indicates that the 90% of the incident EMW can be absorved in between 7.8 GHz and 18 GHz. The minimum reflection loss was observed as -20.0 dB at 10.5 GHz frequency.

6. SUGGESTIONS

In this thesis, the advanced radar absorbing hybrid composites PANI@YIG1-x/CBx (x=0.00, 0.25, 0.50, 0.75 and 1.00) have been synthesized by sol-gel method following in-situ polianiline polimerization process. The structural, magnetic and electromagnetic wave absorbing properties of these advanced materials have been characterized by various techniuqes. The advanced hybrid composites composed of dielectric and magnetic contributions indicate high performance microwave absorption properties. In the scope of the thesis, the advanced radar absorbing hybrid composites have been produced in millimeter thickness range. To be used these materials in military land vehicles; the following works can be studied in the near future for possible defence project.

- The PANI@YIG_{1-x}/CB_x ($0.0 \leq x \leq 1.0$) advanced hybrid composites can be formed at various thicknesses.
- The PANI@YIG_{1-x}/CB_x ($0.0 \leq x \leq 1.0$) advanced hybrid composites can be used as a radar absorbing camouflage paint.
- The hybrid composites can be reinforced with various reinforcement elements to increase the mechanical strength of materials.

REFERENCES

[1] S. Haykin, *Cognitive dynamic systems: perception-action cycle, radar and radio*. Cambridge University Press, 2012.

[2] M. Gupta, "Radar Revisited (review of" Radar Handbook, " by Merrill Skolnik)[Book Reviews]," *IEEE Microwave Magazine*, vol. 9, no. 4, pp. 129-130, 2008.

[3] "Principles and Application System of Radar," ed.

[4] S. Singh, D. Gupta, and V. Jain, "Recent applications of microwaves in materials joining and surface coatings," *Proceedings of the Institution of Mechanical Engineers, Part B: Journal of Engineering Manufacture*, vol. 230, no. 4, pp. 603-617, 2016, doi: 10.1177/0954405414560778.

[5] "Electromagnetic Wave ", ed.

[6] W. D. Callister, "a David G. Rethwisch," *Materials science and engineering: an introduction*, vol. 8, 2010.

[7] Y. Akınay, "Radar Absorbing Composite Materials Production," materials engineering, van yüzüncüyıl üniversitesi, 2018.

[8] "Microwave spectrum with increasing frequencies IGCSE Physics," ed.

[9] T. P. Naik, I. Singh, and A. K. Sharma, "Processing of polymer matrix composites using microwave energy: A review," *Composites Part A: Applied Science and Manufacturing*, vol. 156, p. 106870, 2022/05/01/ 2022, doi: https://doi.org/10.1016/j.compositesa.2022.106870.

[10] D. V. Fitterman, "11.10 - Tools and Techniques: Active-Source Electromagnetic Methods," in *Treatise on Geophysics (Second Edition)*, G. Schubert Ed. Oxford: Elsevier, 2015, pp. 295-333.

[11] P. Saville, T. Huber, and D. Makeiff, "Fabrication of organic radar absorbing materials: A report on the TIF project," *DRDC, Defense R&D Canada, Tech. Rep. Atlantic TR*, vol. 124, p. 2005, 2005.

[12] B. Zohuri, "Stealth Technology," in *Radar Energy Warfare and the Challenges of Stealth Technology*, B. Zohuri Ed. Cham: Springer International Publishing, 2020, pp. 205-310.

[13] Z. S. Normi, "Study of thin resistively loaded FSS based microwave absorbers," 2015.

[14] S. Kangal, *Development of radar-absorbing composite structures*. Izmir Institute of Technology (Turkey), 2013.

[15] F. Ruiz-Perez, S. M. López-Estrada, R. V. Tolentino-Hernández, and F. Caballero-Briones, "Carbon-based radar absorbing materials: A critical review," *Journal of Science: Advanced Materials and Devices*, vol. 7, no. 3, p. 100454, 2022/09/01/ 2022, doi: https://doi.org/10.1016/j.jsamd.2022.100454.

[16] S. M. Abbas, M. Chandra, A. Verma, R. Chatterjee, and T. C. Goel, "Complex permittivity and microwave absorption properties of a composite dielectric absorber," *Composites Part A: Applied Science and Manufacturing*, vol. 37, no. 11, pp. 2148-2154, 2006/11/01/ 2006, doi: https://doi.org/10.1016/j.compositesa.2005.11.006.

[17] K. Gaylor, "Radar Absorbing Materials - Mechanisms and Materials," p. 36, 02/01 1989.

[18] "Camouflage paint effects for military vehicle (FMV defence ındustry)," ed.

[19] Y. H. Cheng, H. Wu, R. G. Zhao, and F. Zhou, "Mechanical characteristics and ballistic behaviors of high strength and hardness armor steels," *Journal of*

Constructional Steel Research, vol. 197, p. 107502, 2022/10/01/ 2022, doi: https://doi.org/10.1016/j.jcsr.2022.107502.
[20] P. Sahoo, L. Saini, and A. Dixit, "Microwave-absorbing materials for stealth application: a holistic overview," *Oxford Open Materials Science*, vol. 3, no. 1, 2022, doi: 10.1093/oxfmat/itac012.
[21] T.-H. Ting and K.-H. Wu, "Synthesis, characterization of polyaniline/BaFe12O19 composites with microwave-absorbing properties," *Journal of Magnetism and Magnetic Materials*, vol. 322, no. 15, pp. 2160-2166, 2010/08/01/ 2010, doi: https://doi.org/10.1016/j.jmmm.2010.02.002.
[22] M. Wang, G. Ji, B. Zhang, D. Tang, Y. Yang, and Y. Du, "Controlled synthesis and microwave absorption properties of Ni0.6Zn0.4Fe2O4/PANI composite via an in-situ polymerization process," *Journal of Magnetism and Magnetic Materials*, vol. 377, pp. 52-58, 2015/03/01/ 2015, doi: https://doi.org/10.1016/j.jmmm.2014.10.066.
[23] M. Akyol, C. Aka, O. İnözü, F. Ö. Alkurt, and M. Karaaslan, "Absorbing the entire X-band via conductive polymer polyaniline coated Y3Fe5O12/NiFe2O4 hybrid composites," *Journal of Materials Science: Materials in Electronics*, vol. 34, no. 6, p. 544, 2023/02/14 2023, doi: 10.1007/s10854-023-09968-6.
[24] C. Aka, O. Akgöl, M. Karaaslan, and M. Akyol, "Broadband electromagnetic wave absorbing via PANI coated Fe3O4 decorated MoS2 hybrid nanocomposite," *Journal of Alloys and Compounds*, vol. 967, p. 171702, 2023/12/10/ 2023, doi: https://doi.org/10.1016/j.jallcom.2023.171702.
[25] M. Altay, F. A. Tekşen, M. Karaaslan, and M. Akyol, "Interfacial effect on the microwave absorption properties in Y3Fe5O12/Fe2O3," *Journal of Magnetism and Magnetic Materials*, vol. 590, p. 171636, 2024/01/15/ 2024, doi: https://doi.org/10.1016/j.jmmm.2023.171636.
[26] "Bragg Law." https://www.xtal.iqfr.csic.es/Cristalografia/parte_05_5-en.html (accessed.
[27] P. Scherrer, "Bestimmung der Größe und der inneren Struktur von Kolloidteilchen mittels Röntgenstrahlen."
[28] J. I. Langford and A. J. C. Wilson, "Scherrer after sixty years: a survey and some new results in the determination of crystallite size," *Journal of Applied Crystallography*, vol. 11, pp. 102-113, 1978.
[29] M. A. Musa, R. a. S. Azis, N. H. Osman, J. Hassan, and T. Zangina, "Structural and magnetic properties of yttrium iron garnet (YIG) and yttrium aluminum iron garnet (YAlG) nanoferrite via sol-gel synthesis," *Results in Physics*, vol. 7, pp. 1135-1142, 2017/01/01/ 2017, doi: https://doi.org/10.1016/j.rinp.2017.02.038.
[30] Majid N. Akhtar *et al.*, "Structural and magnetic properties of yttrium iron garnet (YIG) and yttrium aluminum iron garnet (YAIG) nanoferrites prepared by microemulsion method," *Journal of Magnetism and Magnetic Materials*, vol. 401, pp. 425-431, 2016/03/01/ 2016, doi: https://doi.org/10.1016/j.jmmm.2015.10.060.
[31] H. Tian *et al.*, "ZIF-67-derived Co/C embedded boron carbonitride nanotubes for efficient electromagnetic wave absorption," *Chemical Engineering Journal*, vol. 450, p. 138011, 2022/12/15/ 2022, doi: https://doi.org/10.1016/j.cej.2022.138011.
[32] X. Wang, Y. Lu, T. Zhu, S. Chang, and W. Wang, "CoFe2O4/N-doped reduced graphene oxide aerogels for high-performance microwave absorption," *Chemical Engineering Journal*, vol. 388, p. 124317, 2020/05/15/ 2020, doi: https://doi.org/10.1016/j.cej.2020.124317.

[33] L. Chai *et al.*, "Tunable defects and interfaces of hierarchical dandelion-like NiCo2O4 via Ostwald ripening process for high-efficiency electromagnetic wave absorption," *Chemical Engineering Journal*, vol. 429, p. 132547, 2022/02/01/ 2022, doi: https://doi.org/10.1016/j.cej.2021.132547.
[34] M. Cao, X. Wang, W. Cao, X. Fang, B. Wen, and J. Yuan, "Thermally Driven Transport and Relaxation Switching Self-Powered Electromagnetic Energy Conversion," *Small (Weinheim an der Bergstrasse, Germany)*, vol. 14, p. e1800987, 06/07 2018, doi: 10.1002/smll.201800987.
[35] W.-Q. Cao, X.-X. Wang, J. Yuan, W.-Z. Wang, and M.-S. Cao, "Temperature dependent microwave absorption of ultrathin graphene composites," *Journal of Materials Chemistry C*, 10.1039/C5TC02185E vol. 3, no. 38, pp. 10017-10022, 2015, doi: 10.1039/C5TC02185E.
[36] T. Shang, Q. Lu, L. Chao, Y. Qin, Y. Yun, and G. Yun, "Effects of ordered mesoporous structure and La-doping on the microwave absorbing properties of CoFe2O4," *Applied Surface Science*, vol. 434, pp. 234-242, 03/15 2018, doi: 10.1016/j.apsusc.2017.10.175.
[37] W. Zhang *et al.*, "Preparation of Polyaniline@MoS2@Fe3O4 Nanowires with a Wide Band and Small Thickness toward Enhancement in Microwave Absorption," *ACS Applied Nano Materials*, vol. 1, no. 10, pp. 5865-5875, 2018/10/26 2018, doi: 10.1021/acsanm.8b01452.
[38] D. S. Winatapura, A. Mulyawan, A. A. Wisnu, and Yunasfi, "Synthesis, Structure, Magnetic and Absorption Properties of Nd Doped Y3Fe5O12 Garnets Prepared by Mechanochemical Method," *Key Engineering Materials*, vol. 855, pp. 52-57, 2020, doi: 10.4028/www.scientific.net/KEM.855.52.
[39] H. Wu, G. Wu, and L. Wang, "Peculiar porous α-Fe2O3, γ-Fe2O3 and Fe3O4 nanospheres: Facile synthesis and electromagnetic properties," *Powder Technology*, vol. 269, pp. 443-451, 2015/01/01/ 2015, doi: https://doi.org/10.1016/j.powtec.2014.09.045.
[40] L. Yue *et al.*, "One-pot synthesis CoFe2O4/CNTs composite for asymmetric supercapacitor electrode," *Solid State Ionics*, vol. 329, pp. 15-24, 2019/01/01/ 2019, doi: https://doi.org/10.1016/j.ssi.2018.11.006.
[41] Z. Ye, K. Wang, X. Li, and J. Yang, "Preparation and characterization of ferrite/carbon aerogel composites for electromagnetic wave absorbing materials," *Journal of Alloys and Compounds*, vol. 893, p. 162396, 2022/02/10/ 2022, doi: https://doi.org/10.1016/j.jallcom.2021.162396.